EUROFUSION WPS1-PR(16) 15966

F. Effenberg et al.

Numerical investigation of plasma edge transport and limiter heat fluxes in Wendelstein 7-X startup plasmas with EMC3-EIRENE

Preprint of Paper to be submitted for publication in
Nuclear Fusion

This work has been carried out within the framework of the EUROfusion Consortium and has received funding from the Euratom research and training programme 2014-2018 under grant agreement No 633053. The views and opinions expressed herein do not necessarily reflect those of the European Commission.

Numerical investigation of plasma edge transport and limiter heat fluxes in Wendelstein 7-X startup plasmas with EMC3-EIRENE

F. Effenberg[1], Y. Feng[2], O. Schmitz[1], H. Frerichs[1], S. A. Bozhenkov[2], H. Hölbe[2], R. König[2], M. Krychowiak[2], T. S. Pedersen[2], D. Reiter[3], L. Stephey[4], W7-X Team[2]

[1] Department of Engineering Physics, University of Wisconsin - Madison, WI 53706, USA

[2] Max-Planck-Institut für Plasma Physik, 17491 Greifswald, Germany

[3] Institut für Energie- und Klimaforschung, Forschungszentrum Jülich GmbH, 52425 Jülich, Germany

[4] HSX Plasma Laboratory, University of Wisconsin - Madison, WI 53706, USA

E-mail: effenberg@wisc.edu

Abstract. The results of a first systematic assessment of plasma edge transport processes for the limiter startup configuration at Wendelstein 7-X are presented. This includes an investigation of transport from intrinsic and externally injected impurities and their impact on the power balance and limiter heat fluxes. The fully 3-D coupled plasma fluid and kinetic neutral transport Monte Carlo code EMC3-EIRENE is used.

The analysis of the magnetic topology shows that the poloidally and toroidally localized limiters cause a 3-D helical scrape-off layer (SOL) consisting of magnetic flux tubes of three different connection lengths L_C. The transport in the helical SOL is governed by L_C as topological scale length for the parallel plasma loss channel to the limiters. A clear modulation of the plasma pressure with L_C is seen. The helical flux tube topology results in counter streaming sonic plasma flows.

The heterogeneous SOL plasma structure yields an uneven limiter heat load distribution with localized peaking. Assuming spatially constant anomalous transport coefficients, increasing plasma density yields a reduction of the maximum peak heat loads from 12MWm^{-2} to 7.5MWm^{-2} and a broadening of the deposited heat fluxes.

The impact of impurities on the limiter heat loads is studied by assuming intrinsic carbon impurities eroded from the limiter surfaces with a gross chemical sputtering yield of 2%. The resulting radiative losses account for less than 10% of the input power in the power balance with marginal impact on the limiter heat loads. It is shown that a significant mitigation of peak heat loads, 40-50%, can be achieved with controlled impurity seeding with nitrogen and neon, which is a method of particular interest for the later island divertor phase.

1. Introduction

The quasi-isodynamic stellarator Wendelstein 7-X [1, 2] started the first plasma operation in a limiter configuration [3, 4]. In this field configuration the plasma boundary

does not include magnetic islands and the SOL is defined by five poloidal graphite limiters located at the bean shaped symmetry planes. The limiters define the position of the last closed flux surface and are positioned such that they prevent high heat fluxes onto the unprotected main chamber wall and metallic frame structure of the divertor targets which will be installed later.

Initial discharges are limited to a maximum deposited energy of 400kJ on each limiter (in total 2MJ) at maximum heat loads of 10 MWm^{-2} [3]. The limiter shape was chosen based on a field line diffusion method to optimize the heat load distribution and prevent peak loads P_{peak} from exceeding the design limits at an input power of about $P_{in} = 4$ MW [4].

This limiter configuration was designed to simplify the in-vessel target design and allow for faster startup. Though one might intuitively think that the edge configuration of this limiter configuration is simple, it is shown in this paper that the combination of the particular limiter design and localization with the helicity of the plasma edge topology in the magnetic configuration establishes a 3-D boundary such that the power and particle drain still remains a 3-D edge transport issue similar to the later island divertor configuration [5, 6, 7].

A set of three distinct types of magnetic flux tubes is established in the SOL and hence, from the edge transport point of view, the limiter configuration represents an excellent basic test case for studying 3-D helical SOL transport and the coupling to the main target elements without the complication of magnetic field stochasticity or the effects of finite plasma pressure on the 3-D equilibrium. This predictive study shows that substantial plasma densities and heat loads on the limiters can be reached such that the interaction of the 3-D SOL plasma with the limiters as heat bearing component and the impurity release from these limiters can be assessed.

The results presented contribute also to the exploration of the edge transport and divertor heat and particle loads in the later island divertor phases. Moreover, this magnetic topology is comparable to helical SOL topologies assessed for instance at Tore Supra with the ergodic divertor [8, 9] and TEXTOR-DED [10, 11, 12] as well as the helical divertor structure in the Large Helical Device (LHD) [13, 14] and the quasi-helically symmetric (QHS) configuration of the Helically Symmetric eXperiment (HSX) [15, 16].

Power losses due to edge impurity radiation are expected to be crucial during future high-heat-flux divertor campaigns and quasi-stationary high performance operation [17, 18, 19]. The approach is to use intrinsic and actively injected impurity species in the edge plasma to radiate energy and reduce the heat flux reaching plasma facing components (PFCs). This has been shown to be succesful at other devices in the past [20, 21, 22, 23, 24, 25, 26, 27]. In particular the investigation of the effects of the magnetic edge topology on the stability of detachment and radiation layer at Tore Supra [28] and W7-AS [29, 30] and recent achievements of detachment stability at LHD using external gas fueling combined with resonant magnetic perturbations [31] show the potential to enhance the plasma performance and enable full exploitation of the steady

state capabilities of W7-X.

In this paper, a first systematic numerical exploration of the plasma edge transport and plasma surface interaction (PSI) for scenarios during the startup phase of W7-X (OP1.1) [3] is presented. The aim is to provide first predictions and a general overview of the plasma edge transport behavior, the limiter heat loads and the impact of intrinsic and seeded impurities on the power balance. In the latter case the focus is on the exploration of controlled radiative edge cooling. This study does not aim for completeness, rather serves to motivate experiments and to provide a first approach for the interpretation of the relevant and most obvious 3-D SOL physics effects. Future studies will go deeper into those aspects which turn out to be relevant and accessible by diagnostics during the relatively short initial experimental campaign [3, 32, 33].

The inherent non-axisymmetric magnetic field configuration and the limiters exposed to the plasma acting as strong recycling and intrinsic impurity sources require self-consistent 3-D modeling of at least plasma and neutral transport. For this purpose the fully 3-D coupled fluid plasma edge and kinetic neutral transport Monte Carlo code EMC3-EIRENE [34, 35] is employed in this study. EMC3 was originally developed for stellarators and solves a set of reduced Braginskii fluid equations for particles, parallel momentum, and energies for electrons and ions [36]. The parallel heat transport is classical while the perpendicular transport of particles and heat is assumed to be anomalous and has to be set as input parameters $D_\perp$ and $\chi_{\perp,e,i}$. At the surfaces of simulated PFCs Bohm boundary conditions are applied for particle and heat fluxes.

EIRENE solves the kinetic transport equations for neutral atoms and molecules including collisional processes [37, 38]. It provides ionization sources, momentum and energy sources and sinks from the atomic and molecular processes such as charge exchange and ionization.

The impurity transport is modeled by a trace fluid approach which assumes only a small density perturbation by the impurities. A simplified fluid momentum balance equation is solved and the impurities impact the main plasma species only by ionization and excitation through a loss term in the energy balance equation [39].

Self-consistent treatment of magnetic or electric drift effects and volumetric recombination are not included in the current code version.

The scenarios adressed and the boundary conditions used are explained in further detail in section 2.

The edge topology is analyzed in section 3 in order to investigate the magnetic field structure and the target-to-target connection lengths L_C as an important topological quantity for the edge transport.

In section 4 the correlation between the magnetic topology and plasma edge transport is discussed.

The PSI is considered in section 5 by calculating the limiter heat fluxes and relating their characteristic pattern to field topology and the impact of different transport conditions. Parameter scans with respect to density and perpendicular transport coefficients are performed in order to investigate their impact on the plasma edge

transport and power deposition on the limiters.

In section 6 radiative edge cooling is modeled taking carbon sputtering proportional to the incoming bulk ion flux into account.

Radiative power losses from actively seeded nitrogen and neon are considered in section 7. The impact of impurity radiation is primarily investigated with respect to heat flux mitigation.

In section 8, the results are summarized and next steps for future work are presented.

2. Modeling boundary conditions for the limiter scenario

The magnetic field configuration and the shape of five inboard graphite limiters are chosen for the startup scenario [4] such that significant power loads to the metallic in-vessel components are avoided and a limiter heat load distribution is achieved which is as homogeneous as possible. A complete vacuum Poincaré plot calculated at the bean shaped symmetry cross section ($\phi_{tor} = 0°$) is shown in figure 1a. In figure 1b the impact of the limiters is sketched. The limiters have a vertical extension of about ΔZ ≈90cm and and toroidal extension of ΔY ≈18cm ($\Delta\phi_{tor}$ ≈1.9°). They define the magnetic SOL topology by cutting the field lines in a domain featuring mostly closed magnetic flux surfaces. The resulting poloidally alternating pattern in the profile shown in figure 1b represents the open field lines featuring three different lengths: L_C =36m, 43m and 79m. This will be further assesed in section 3. The $\iota = 5/5$ divertor islands are shifted far outside of the limiter radius (not included in the Poincaré plot), while the $\iota = 5/6$ resonance is located within the LCFS. As a result any short circuiting within the edge transport region by fast transport around island separatrices is avoided.

Taking into account the five-fold periodicity and the stellarator symmetry of W7-X [40] a simulation grid covering a toroidal extension of $\Delta\phi_{tor} = \frac{1}{2} \cdot \frac{360°}{5} = 36°$ is sufficient for EMC3-EIRENE simulations to assess the plasma edge features. A density scan is performed varying the last closed flux surface densities n_{LCFS} between $1{\cdot}10^{18}\mathrm{m}^{-3}$ and $1.9{\cdot}10^{19}\mathrm{m}^{-3}$ for a fixed heating power of P_{in} = 4 MW which is defined at the inner simulation boundary (ISB, not identical with LCFS). Some dedicated cases are investigated with a reduced power of 2MW.

The anomalous transport coefficients are free model parameters which are in general unknown and can be inferred experimentally [41]. For now, they are assumed to be spatially constant and kept fixed for this study at values of $D_\perp$ =1 $\mathrm{m}^2\mathrm{s}^{-1}$ and $\chi_{\perp,e,i}$ =3$D_\perp$ for both, hydrogen and impurity species. They were varied in some cases in order to study the dependence of the edge transport and resulting heat loads on the level of cross field transport.

The production of intrinsic carbon impurities is modeled by a gross sputtering yield of Y_{chem} =0.02. This corresponds to a carbon flux of 2% of the recycling flux to mimick the chemical erosion. Once released from the limiters, the neutral impurities are traced kinetically until ionized and then the resulting impurity ions are followed by the fluid ion

tracing method in EMC3 through the plasma. Assuming a small density perturbation, the impurities interact with the background plasma only through a loss term in the energy balance equation.

Local gas sources are defined according to the experimentally available high pressure gas injection systems [3, 32] and appropriate injection currents $I_{N,Ne}$ are chosen as a free parameter in order to model controlled seeding of nitrogen and neon. A radiation fraction of 40% of the input power entering the inner simulation boundary is targeted in this study in order to achieve a significant impact on the limiter heat loads which should also be observable by diagnostics available during the startup phase. By default, impurities reaching the inner simulation boundary are returned from the core domain in the same charge state as they entered. In addition, in order to examine possible effects of the core transport conditions on the plasma edge impurity transport, a 1-D core transport model [42] is applied for a specific case study. This model takes further ionization of impurities crossing inside the core plasma into account.

3. Limiters cause non-isotropic SOL topology of helical flux tubes

The magnetic topology is analyzed by calculating the target-to-target field line connection lengths L_C which define characteristic parallel transport length scales of the helical flux channels. The results are shown in figure 2 as 2-D connection length profiles $L_C = L_C(R, Z)$ at four toroidal cross sections. In figure 2a the up/down-symmetric bean shaped section at $\phi_{tor} = 0°$ is shown where the limiter is located. The cross section including the location of the gas injection system at $\phi_{tor} = 12.3°$ is shown in figure 2b. A further loaction at $\phi_{tor} = 24°$ is shown in figure 2c. The triangle shaped symmetry section at $\phi_{tor} = 36°$ is shown in figure 2d.

A clear poloidal modulation of L_C is seen which results from the interaction of the limiters with helical field lines at low magnetic shear. It is found that the SOL magnetic topology composes of three types of magnetic flux tubes of different L_C.

The reason for their formation is explained in figure 3 where the 3-D paths of three single field lines, each as representative of one magnetic flux tube, are shown. In the first case, the field line starts and ends at the same limiter after one toroidal turn (figure 3a), corresponding to a length of $L_C \approx$36m. In the second case the field line hits after 1.2 toroidal terms the next neighbouring limiter, corresponding to $L_C \approx$43m (figure 3b). In the last case the field line needs 2.2 toroidal turns ($L_C \approx$79m) to reach the next neighbouring limiter (figure 3c). The outer layer of L_C in the very edge has a neglible impact as it lies several density decay length radially outward of the real SOL transport domain. As a consequence, the wall and in-vessel componentes are neglected as targets in this topological analysis and the following transport calculations.

From figure 3 it is obvious that every limiter is connected with itself by the shortest flux tube (36m) and with the next neighbouring limiters by the longer ones (43m and 79m). The SOL magnetic topology relevant for transport decomposes therefore into $3 \cdot 5 = 15$ separate magnetic flux tubes.

In summary, the W7-X start-up topology features a relatively simple discrete distribution of connection lengths due to low shear, sufficiently poloidally extended limiters and the absence of strong resonances in the edge. This is in contrast e.g. to the ITER limiter topology [43, 44], which features very complex patterns of radially and poloidally separated domains of L_C which vary over several orders of magnitude.

4. Poloidal modulation of pressure profiles and counter streaming flows

EMC3-EIRENE simulations were carried out for pure hydrogen plasmas at spatially fixed perpendicular transport coefficients ($D_\perp$=1 m^{2}s^{-1}, $\chi_{\perp,e,i}$=3$D_\perp$) and P_{in}=4MW. The resulting SOL plasma transport profiles show for all density cases a strong poloidal modulation of the plasma parameters.

This is shown in figure 4 for a scenario with n_{LCFS} =7·10^{18}m^{-3} at P_{in} =4MW. The 2-D profile of the thermal plasma pressure ($p = n(T_e + T_i)$) in figure 4a features dented isobares. A comparison with figure 2b reveals that the poloidal variations of the pressure follow the connection length modulation. Poloidal scans of plasma data and connection lengths along poloidal surfaces of constant effective radii show a clear correlation between plasma transport and magnetic edge topology. In figure 4b such a 1-D poloidal profile is shown for SOL pressure (red) and L_C (blue). The maxima and minima of the pressure clearly match with the maxima and minima of the connection lengths.

The 2-D Mach number profile in figure 4c features a poloidal modulation and counter streaming flows in neighboring flux channels in correlation with the connection length profiles in figure 2b. In figure 4d the corresponding 1-D poloidal SOL profiles are shown for Mach number (green) and L_C (blue). The plasma flow shows a strong modulation in correlation with the lengths of the respective magnetic flux bundles.

The poloidal pressure variations manifest because the long connection length flux channels show higher densities and temperatures due to stronger cross field fueling of particles and heat from the confinement and the longer parallel transport length scales when compared to the shorter ones. In the short connection lengths regions the fast parallel losses are more effective. This modulated pressure (figure 4a,b) drives the corresponding flows (figure 4c,d).

The counter streaming flows at a given toroidal location (here $\phi_{tor} = 12.3°$) arise because the adjacent helical transport channels are of different lengths (L_C) and are partly connected to different limiters. Therefore the midpoints ($l_\parallel = \frac{L_C}{2}$ if $l_\parallel \in [0, L_C]$ measures the magnetic limiter-to-limiter distance) which are in the simple SOL model [45] assumed to be the locations of the stagnation points ($v_\parallel$ =0 ms^{-1} and M =0) are shifted with respect to each other. Within a single flux tube the flow strength increases once one leaves the midpoint along $l_\parallel$ either in positive or negative toroidal direction towards the connected limiters. The direction and level of sonic flow depends on the distance to the closest limiter where it reaches ion sound speed (M=1) - in EMC3-EIRENE, the Bohm velocity is used as boundary condition at the target.

An interpretation by the simple SOL model may hold as a first approximation for the interpretation of the 3-D simulation results. The development of corresponding simple models for the 3-D SOL of stellarators is an ongoing task of research. E.g. the assumption of the simple SOL model that all ionization occurs inside of the last closed flux surface is not necessarily valid since the helical flux tubes in the W7-X startup configuration studied pass the vincinity of other limiters and therefore can receive neutral particle sourcing from additional recycling neutrals within the EMC3-EIRENE model. These additional ionization sources might slightly change the flow structure expected from a simple SOL description in the given cases. For the time being, the simple SOL approach is used as an initial guideline. In the following the correlated impact of the heterogenous L_C topology on the limiter heat loads will be discussed.

5. The 3-D helical SOL topology causes uneven limiter heat loads

In the following the limiter heat loads of hydrogen plasmas are analyzed with particular focus on the correlation to the magnetic topology. Effects of impurities will be discussed separately in the next sections.

As a first step the connection lengths mapping and the limiter heat loads q_{depo} are calculated with EMC3-EIRENE. In figure 5 the 2-D L_C mapping (left) and the resulting 2-D distributions of the heat load for the density case n_{LCFS} =1·10^{18}m^{-3} at an input power of P_{in} =4MW (right) are shown. The connection lengths pattern consists of diagonal red stripes corresponding to the long (79m) magnetic flux tubes. The dark blue center stripe represents a region without magnetic connection because of the flat top of the limiter. Here the field lines of the LCFS proceed tangential towards the limiter. The size of the unwetted area in the modeling might be slightly overestimated because of the finite radial resolution of the numerical grid used for the L_C mapping. The dark blue unwetted region and the red stripes enclose the domain of 43m long connection lengths (green). The outer (turquoise) area corresponds to the shortest length scale (36m).

A characteristic feature of the heat flux pattern shown in figure 5 (left) are the vertical stripes with maxima $P_{peak} = max(q_{depo})$ on the upper left and lower right part of the limiters ($Z \approx +/- 0.2$m). These striation patterns result as a combined effect of magnetic flux tube topology, target geometry, incident angles of the field lines and the radial decay of plasma transport. The heat loads reduce towards the outer part of the limiters, as the parallel heat fluxes decay exponentially in radial direction. Due to the missing magnetic connection no fraction of $q_{||}$ reaches the flat center of the limiter. Rather one would expect a weak diffusive cross field transport contribution to q_{depo} at this small flat domain. However, this perpendicular depostion is neglected at this point since it is not relevant for the heat flux characteristics defined and discussed in the following.

Electrons lost along the open field lines towards the limiters will establish the parallel temperature and density gradients in the code (using ambipolarity condition) and these parallel gradients will cause convective and conductive heat fluxes onto the

limiters. According to the correlation between plasma parameter and magnetic length scales L_C, the P_{peak} appear at positions where the long flux tubes connect to the limiters close to the LCFS (at $Z \approx +/-0.2$m in figure 5). As in the case of the pressure and flow modulations correlated to L_C before (section 4), this is because the long magnetic flux tube receives more cross field fueling of particles and heat which corresponds to a higher ratio of perpendicular to parallel transport. This correlation however is effective only in the near SOL region where the flux tubes touch the LCFS and receive cross field fueling from the confinement region. In the far SOL this correlation gets washed out since the flux tubes overlap in radial direction in the outer SOL and exchange particles and heat among eachother.

For tokamaks, it was found that the heat flux channel width scales with the poloidal magnetic field and hence results for ITER in very small values causing a strong concentration of heat loads on divertor target tiles [46, 47]. For stellarators it is assumed that the much longer connection length (e.g. several 100m for the island divertor SOL [18]) will result in a significant broadening of the heat flux channel width. The helical SOL of the W7-X startup scenario allows to assess this initially, though the previous discussed magnetic connection lengths are in a range close to those in a tokamak SOL.

The limiters of the W7-X startup configuration feature a 3-D shape such that effects of the target geometry function on the deposited heat fluxes have to be considered carefully. In order to define a measure for the heat load decay in relation to the SOL heat flux channel width, a description of the deposited heat flux distributions and explanation of governing mechanisms is attempted in the following. The parallel heat flux reaching the limiter is defined as:

$$q_{\parallel} = nc_s(\gamma_e T_e + \gamma_i T_i) + q_{rec} \tag{1}$$

where γ_e =4.5 and γ_i =2.5 represent the sheath heat transmission coefficients for electrons and ions and $c_s \approx \sqrt{\frac{T_e+T_i}{m_i}}$ is the ion sound speed. The additional term q_{rec} =(13.6eV +2eV)nc_s accounts for a small heat flux contribution due to atomic and molecular recombination on the limiter surface. The parallel heat flux $q_{\parallel}$ is assumed to decay radially as:

$$q_{\parallel} = q_{\parallel,0} e^{-(r-r_{LCFS})/\lambda_{q_{\parallel}}} \tag{2}$$

where $\lambda_{q_{\parallel}}$ is a chracteristic decay length and r is the effective radius. Taking modification by geometry effects into account, the deposited heat flux on the limiter is given by:

$$q_{depo} = q_{\parallel} \sin(\alpha) = q_{\parallel,0} e^{-(r-r_{LCFS})/\lambda_{q_{\parallel}}} \sin(\alpha) \tag{3}$$

where α is the incident angle of a field line on the limiter. The limiter surface is formed in such a way that α mainly depends on r. This assumption is based on the design of the limiter surface which was adjusted such that it lays conformal to an idealized LCFS [4]. In this idealized assumption, the deformation of a surface element with length s along the limiter surface is just a function of the radius and not of the

poloidal angle. The local surface coordinate s is here defined such that $s(r_{LCFS}) = 0$ and $|s|$ increase in toroidal direction (compare to magenta mark in figure 6(left) and horizontal axis in figure 6(right) in the following). At the limiter tip ($s = 0$) α is zero, hence $q_{depo} = 0$. The changes of the q_{depo} profiles along the limiter surface can be explained by calculating the first derivative of q_{depo} with respect to s:

$$\frac{dq_{depo}}{ds} = q_{\parallel}\cos(\alpha)\frac{d\alpha}{dr}\frac{dr}{ds} - \frac{1}{\lambda_{q_{\parallel}}}q_{\parallel}\sin(\alpha)\frac{dr}{ds} = (\frac{1}{\lambda_{\alpha}} - \frac{1}{\lambda_{q_{\parallel}}})\frac{dr}{ds}q_{depo} \tag{4}$$

where $\lambda_{\alpha} = \frac{\tan(\alpha)}{\frac{d\alpha}{dr}} > 0$ being a purely geometric factor. Thus, q_{depo} has maxima at $\lambda_{\alpha} = \lambda_{q_{\parallel}}$. On the limiter-tip side of the maximum (the flat limiter center domain), where $\lambda_{\alpha} < \lambda_{q_{\parallel}}$, $\frac{dq_{depo}}{ds}$ is mainly determined by the limiter surface form. Here, the sudden strong decay behaviour of the q_{depo}-profiles around the limiter center is caused by the shallow angle of incidence ($\alpha \to 0$). In the limiter edge regions the field lines terminate with a steeper angle of incidence on the limiter surfaces and $\lambda_{\alpha} \gg \lambda_{q_{\parallel}}$. Here, the limiter heat load q_{depo} is less affected by the target geometry and can therefore serve to estimate the strength and decay of the actual parallel heat flux $q_{\parallel}$. That is the peaks and outer tails of the q_{depo}-profiles can be used to illuminate the correlation between magnetic topology and parallel heat fluxes causing explaining the deposition pattern in figure 5 (right).

The dominant role of $\lambda_{q_{\parallel}}$ in the decay of q_{depo} in the limiter edge region enables a characterization of the heat transport by measuring the decay length λ_{sf} which is defined as

$$\lambda_{sf} := -\frac{q_{depo}}{\frac{dq_{depo}}{ds}} \approx \lambda_{q_{\parallel}}\frac{ds}{dr} \tag{5}$$

Because $\frac{ds}{dr}$ is a sensitive function of r, it is expected that the λ_{sf}, deduced by exponentially fitting the q_{depo} profile, is sensitive to the selection of the s-position where the fitting is made.

Additionally, one has to take into account from which L_C domain the local q_{depo} originates. From figure 5 it is clear that one might cross different magnetic flux tubes while following an arbitrary path in s-direction along the limiter surface. The definition of λ_{sf} provided above is therefore valid for each L_C separately. It is a quantity which is measured experimentally and can be compared with the values obtained from numerical simulations. An attempt to map the surface fluxes inferred from EMC3-EIRENE modelling to the upstream position is ongoing and will be presented in future publications as separate topic.

In order to study the dependence of the parallel heat fluxes on changing plasma transport conditions, a density scan is performed. In figure 6(left) the resulting 2-D heat flux distributions on the limiter surface are shown for densities in the range of n_{LCFS} =1·10^{18}-1.9·10^{19}m^{-3} at a fixed input power of P_{in} =4MW. Profiles along the limiter surface path length s in horizontal direction are extracted at the position of the peak value in the right deposition stripe ($Z \approx -0.2$m) for the different n_{LCFS}. These

1-D surface heat flux profiles $q_{depo}(s)$ are overlaid with the connection lengths L_C as shown in figure 6(right). Due to the geometry effects discussed above, the 1-D profiles exhibit steep decay towards the center domain of the limiter and shallower decay in the outer part of the limiter.

The heat flux characteristics for the density scan are shown in figure 7. The heat load maxima (P_{peak}) obtained from the left and right peak profiles (figure 6) are plotted for the different densities in figure 7(left). The effective λ_{sf} of the tails of the left and right peaks are shown in figure 7 (right). In order to reduce the effects of the target geometry and keep them separated by the magnetic connection lengths L_C as discussed above, the λ_{sf} are determined by exponential fits of the left and right 1-D peak profile tails marked in red, (figure 6 (right). The left left tail features a slightly higher λ_{sf} than the right tail (a factor of ≈1.3) as seen in figure 7(right).

With an increase in n_{LCFS} of approximatly one order of magnitude from $1{\cdot}10^{18}\mathrm{m}^{-3}$ to $1.9{\cdot}10^{19}\mathrm{m}^{-3}$, the maximum peak loads reduce from P_{peak} ≈12.5MW to ≈7.5MW on the right profile and from P_{peak} ≈9.5MW to P_{peak} ≈7MW on the left profile. The decay increases for the right profile tail by a factor of two from λ_{sf} ≈0.75cm to ≈1.5cm. The left profile tail increases by approximatly the same factor from λ_{sf} ≈1cm to ≈2.1cm. This is because with rising density the fixed input power is distributed among more plasma particles and perpendicular fueling of the flux tubes is increased. At the same time the power losses due to the interaction with neutrals drop from 11.2% to 7.5-8.5%. Here, the term of the anomalous perpendicular heat flux becomes more effective due to its dependence on the density n:

$$q_\perp = \chi_{\perp,e,i} n \nabla_\perp T_{e,i} + \frac{5}{2} T_{e,i} D_\perp \nabla_\perp n \tag{6}$$

The leading term behind this finding is within the EMC3-EIRENE model equations the density dependence of the perpendicular conductive heat transport shown in equation 6. In addition to the increasing density, an effect of reduced temperature under fixed power input is expected from the convective and conductive terms in equation 6. While the density is increased by one order of magnitude at the upstream position, the temperature is only reduced by 16%. This results in the decay of P_{peak} (figure 7,left) and broadening of $\lambda_{q_\parallel}$ (figure 7, right). However, the change of maximum peak levels and distribution widths in the deposition profiles in figure 6 and the heat flux characteristics in figure 7 decreases with further increasing n_{LCFS}. So far, the anomalous cross-field transport coefficients were kept to be $D_\perp = 1.0\ \mathrm{m}^2\mathrm{s}^{-1}$ and $\chi_{\perp,e,i} = 3D_\perp$. They have to be inferred experimentally.

To consider their impact on the target heat load distribution, transport coefficient scans are performed for n_{LCFS}=$9{\cdot}10^{18}\mathrm{m}^{-3}$. Furthermore, this diffusion scan is performed at low and high input powers of P_{in} =2MW and 4MW. The resulting 2-D limiter heat loads for $D_\perp = 0.5\mathrm{m}^2\mathrm{s}^{-1}$, $1.0\mathrm{m}^2\mathrm{s}^{-1}$ and $2\mathrm{m}^2\mathrm{s}^{-1}$ are shown in figure 8(left) for P_{in} =2MW. The corresponding 1-D profiles are shown in figure 8 (right) for both heating scenarios. The blue, cyan and green curves correspond to increasing transport coefficients at P_{in} =4MW while magenta, red and yellow correspond to the same coefficients at

P_{in} =2MW. The reduction of the input power by a factor of 2 causes nearly a halving of the peak maxima. However, in both input power cases P_{peak} strongly varies with $D_\perp$ as well.

In the heat flux characteristics in figure 9, the drop of P_{peak} as result of reduced input power and the decay with increasing $D_\perp$ is shown. Green symbols represent the high input power (P_{in} =4MW) maximum peaks and effective λ_{sf} obtained from left and right peaks by the same fitting method as in the density scan above. The blue symbols correspond to the same data obtained at P_{in} =2MW. The evolution shows very clearly a broadening of the heat channel and a decay of the maximum peak in the two scenarios. The perpendicular convective and conductive heat flux in equation 6 is in this case increased through the rising $\chi_{\perp,e,i}$ and $D_\perp$ respectively.

The decay of the right peak maximum P_{peak} by ≈40% and the increase of the related λ_{sf} by a factor of 2-3 for rising $D_\perp$ emphasizes the importance of carefully choosing the experimentally inferred transport parameters used as modeling input. In turn, by matching the experimental profiles with the model, $D_\perp$ and $\chi_{perp,e,i}$ can be inferred. A mapping of the parallel heat flux from the downstream to the upstream position and a more detailed analysis of the transport dependence on L_C is subject of ongoing research.

Of course, the effects of error fields and changes of the vacuum magnetic field due to electro-magnetic forces acting on the coil geometry can slightly change the magnetic topology and the correlated strike lines. More obvious changes could arise due to drift effects such as $\propto \vec{E} \times \vec{B}$ not included in the current version of EMC3-EIRENE.

A substantial underestimation of the modeled heat loads onto the limiter center tangential to the magnetic field lines of the LCFS is due to the assumption that only $q_\parallel$ contributes to q_{depo}. As discussed in [44, 48] substantial loads up to 10% of $q_\parallel$ can appear on PFCs oriented parallel to B in tokamak experiments. For the stellarator non-zero contributions due to funneling might therefore modify the predicted heat load patterns in the center.

6. Effects of eroded intrinsic impurities

The helical SOL transport studies discussed so far did not take impurities into account. Impurity transport is addressed in this section with the particular focus on the impact of impurity radiation on the limiter heat loads. The experience gathered should be useful for later investigations of this topic in the topologically more challenging island divertor scenarios. In this section the impact of intrinsic carbon impurities eroded from the limiters is assessed in order to estimate the amount of total radiative losses and the relevance for edge cooling.

With a fixed effective sputtering yield of 0.02, the resulting gross erosion of carbon yields impurity fluxes between $2.8{\cdot}10^{20}$at/s and $3.2{\cdot}10^{21}$at/s for the given density range, leading to total radiative losses of 0.03 MW to 0.28 MW in the complete simulation domain. This corresponds to a fraction of less than 7-8% of the input power in the

investigated transport domains. The effective yield assumes that chemical erosion is dominant. Physical sputtering which depends on the energies of the hitting particles [45] is neglected so far. Because this study focuses on the feasibility of edge cooling, radiative losses from heavier impurities (in particular iron, copper) are not taken into account. High energetic charge exchange neutrals born in the confinement region and rarely affected by the SOL temperature and density conditions could sputter significant amounts of heavy impurities at the metallic wall and other in-vessel components, as discussed in [49]. In the consequence the radiative losses by heavy impurities could set a density limit and restrict the maximum operational n_{LCFS} below the maximum value ($1.9{\cdot}10^{19}\mathrm{m}^{-3}$) assumed in this study.

An overview of the total impurity radiation distribution for a density scenario of n_{LCFS} =$1.3{\cdot}10^{19}\mathrm{m}^{-3}$ at P_{in} =4MW at the toroidal cross section of the gas inlet is provided in figure 10. In figure 10a only the integrated carbon impurity radiation is shown, while figures 10b and c contain the total radiation during nitrogen and neon seeding scenarios which will be discussed in the next section. The carbon radiation is primarily located near the LCFS, peaking within the SOL. In figure 10a the radiation pattern contains a stripe-shaped domain of high intensity corresponding to the shadow of a limiter, from where the carbon originates.

In figure 11 the poloidally and toroidally averaged radial distributions of the total impurity radiation for four density scenarios are shown. The density dependence of the radial carbon radiation distribution for the four density cases is provided in figure 11a. For the densities with n_{LCFS} >$7.0{\cdot}10^{18}\mathrm{m}^{-3}$, the peak values of the total carbon radiation are located in the SOL at an effective radius of $r_{eff} \approx 50$ cm, 2-3 cm distant from the LCFS. The highest density (n_{LCFS} =$1.9{\cdot}10^{19}\mathrm{m}^{-3}$) causes obviously the highest chemical sputtering and therefore the highest radiation amount (cyan line in figure 11a) with a peak value of $P_{rad,C,max}$ ≈$0.11\mathrm{Wcm}^{-3}$.

However, the choice of the transport coefficients and the boundary conditions for the impurities can change the results. In order to assess these issues, both, the boundary conditions at the LCFS and the cross-field transport coefficients are varied for carbon in the following for a fixed n_{LCFS} =$9{\cdot}10^{18}\mathrm{m}^{-3}$ with P_{in} =4MW. The resulting radial radiation profiles are shown in figure 11b.

In the previous default cases the transport parameters were kept spatially constant at $D_\perp = 1.0\mathrm{m}^2\mathrm{s}^1$, $\chi_{\perp,e,i} = 3D_\perp$ inside and outside the LCFS and the inner simulation boundary condition is set such that the net impurity ion flux for each charge state is zero. The resulting radiation distribution is shown in figure 11b (blue); in this case, about 50% of the total radiative losses occur in the confinement region. This is because the intermediate charge states are not further ionized within the domain enclosed by the ISB. This boundary condition likely overestimates the amount of intermediate charge states and their contribution to radiative losses within the confinement region.

To explore the sensitivity of the impurity results on the boundary conditions, a 1-D impurity transport core model [42] is applied assuming a flat core profile of $n_{core} = 5.0{\times}10^{19}\mathrm{m}^{-3}$, $T_{e,core} = 2.0$ keV and $D_{\perp,core} = 0.1\mathrm{m}^2\mathrm{s}^{-1}$. The resulting profile in figure

11b (red) shows a strong reduction of radiated power in the confinement region; in this case, the radiation at the ISB drops from $P_{rad,C}$ ≈0.025Wcm^{-3} to $P_{rad,C}$ ≈0.007Wcm^{-3}. This is because the core transport model allow for further ionization steps to take place, for C^{+5} in particular. In the default case further ionization of this charge state within the core is neglected which causes an overestimation of its density around the ISB and related contributions to the total impurity radiative losses. However, the peak and the radial distribution of the total impurity radiation within the SOL is not affected by these boundary conditions.

The transport coefficients within the LCFS are expected to show a radial decay in inward direction. Therefore two further cases (magenta and green in figure 11b) are presented assuming different perpendicular transport coefficients for the SOL and confinement region. A radial core transport profile is defined as: $D_\perp(r) = 0.1\text{m}^2\text{s}^{-1}$ for $r < r_{LCFS}$ and $D_\perp(r) = 1.0\text{m}^2\text{s}^{-1}$ for $r \geq r_{LCFS}$ ($\chi_{\perp,e,i}(r) = 3D_\perp(\text{r})$). In the first case (magenta) these profiles are assumed for the main hydrogen species only while the coefficients are kept spatially constant for carbon at $D_\perp$ =1m^{2}s^{-1}. In the second case (green) these profiles are used for both main hydrogen plasma and carbon impurities. In the first case the radiation distribution within the SOL hardly deviates from the cases (blue and red) discussed above. However, it features higher radiative losses in the confinement domain than the remaining cases discussed here. In the second case (green) the radiation has another peak in the confinement domain and then reaches at the ISB the level of radiation obtained by applying the core transport model (red) discussed above. Additionally, the sharp transition of the perpendicular transport applied to the impurities causes a further peak at the LCFS and a slightly increased peak within the SOL. The radiation distribution depends non-linearly on the temperature profile [50] which changes with varying transport conditions as well. The main result obtained is that the SOL radiation is relatively independent of the transport conditions in the confinement and core domain for spatially fixed cross field transport of the impurities. The last case (green) discussed demonstrates a stronger sensitivity of the SOL radition to changes of the perpendicular transport of the impurities.

To examine the impact of carbon erosion on the limiter heat loads, only spatially fixed transport coefficients ($D_\perp = 1.0\text{m}^2\text{s}^{-1}$) are used. This is performed as a first step as the exact conditions in the experiment are unknown and the analysis above has shown that impurity transport and the radiation distribution in the SOL and in the vincinity of the LCFS is barely affected by the changes of the core transport conditions. In figure 12 (left) the 2-D heat flux deposition patterns are shown for the case of pure hydrogen and for cases including impurities at P_{in}=4MW and n_{LCFS} =7·10^{18}m^{-3}. Comparing the two cases, with and without the effects of eroded carbon show only marginal changes in the 2-D profiles. The corresponding 1-D profiles (blue and cyan) in figure 12(right) deviate only slightly in their maximum peak levels. Comparing the surface deposition decay lengths λ_{sf} inferred and the maximum peak loads P_{peak} in the heat flux characteristics in figure 14 (blue and green symbols) confirms that the contribution of intrinsic carbon impurities to heat flux mitigation causes reductions of less than 10% between the peak

load maxima while changes of λ_{sf} are almost undetectable.

The modeling results presented within these boundary conditions show that carbon sputtered from the graphite limiters has only a small capacity for self-protection in terms of power dissipation. Accordingly the sputtered carbon level in the parameter region assessed does not provide a sufficient energy sink to cause plasma termination before possible heavier impurities sputtered from the main vessel wall become relevant [49]. Furthermore, the results clearly show that the edge impurity transport behaviour is, within the assumptions of this study, almost independent from the core transport conditions.

7. Radiative edge cooling by seeded impurities

The helical SOL in the W7-X limiter startup scenario is an excellent test case for the feasibility of radiation cooling in a helical boundary by active gas fueling of suitable radiator gases. The critical question is if the combined effects of gas feed locations in the 3-D boundary, transport and recycling behavior of the injected impurities toghether will allow the injected cooling gases to distribute in a way that they cause a homogenous power dissipation in the plasma edge and reduce the heat fluxes onto PFCs in a controlled and homogenous way.

Two different species are considered for controlled radiative edge cooling by active impurity seeding: nitrogen and neon. The anomalous transport conditions for main plasma and impurities are kept spatially constant at $D_\perp$ =1 $\mathrm{m^2 s^{-1}}$ and $\chi_{\perp,e,i}$ =3$D_\perp$. A density scan is performed prescribing a total power loss of 40% of the input power (4MW) by the respective seeded species, that is $P_{rad,N,Ne}$=1.6MW. At the same time, carbon erosion is assumed at the fixed yield of 0.02 as described in section 6 so that the total radiative losses are caused by intrinsic and externally seeded impurities together. Gas sources are assumed at 10 toroidal positions, each localized at a distance of $\Delta\phi_{tor} \approx +/-$ 12.3° from the bean shaped symmetry planes (figure 2b). This is the planned setup which is presently being developed for the high heat flux divertor phase of W7-X. The kinetic start energy of the impurities is set to 0.05eV in the modeling assuming purely thermal neutral atoms. Reflection, recycling or sputtering of nitrogen and neon is neglected at this point. These assumptions are used in order to provide a first estimate for the radiation distribution edge cooling feasibility and efficiency of these two species. Seeding experiments with these two species showed that neglection of nitrogen recycling on carbon surfaces can be a valid assumption while neon was observed to show stronger recycling and therefore more homegenous and longer lasting radiation distributions [25, 27].

The 2-D radiation patterns of nitrogen and neon (including also the radiation from eroded carbon) are shown in figure 10b, c for the scenario discussed in section 6. The radiation distribution of the seeded impurities suggests strong accumulation behavior inside of separate domains. This is because the impurities are injected into the L_C =43m flux tube (compare green mark in figure 2b). Due to the relatively short L_C,

perpendicular transport does not yield significant fueling of neighbouring flux tubes. This localization of the radiation in the vincinity of the seeded magnetic flux bundle could be disadvantageous for the desired uniform heat load mitigation if the toroidal distribution of local seeding sources is limited and does not match with the periodicity of the helical magnetic topology. During the initial limiter operation scenarios, two of the later planned 10 toroidally symmetric distributed gas injection systems are used for testing controlled impurity seeding and radiation cooling. Local seeding of a magnetic flux tube by a single gas source allows for investigation of the SOL flux tube geometry and possible local source effects. Comparisons of experimental results to the modeling results presented here are ongoing.

An example of the 2-D limiter heat load distributions including the mitigation effects of nitrogen and neon impurities (and simultaneous carbon erosion) is shown in figure 12 (left), and as 1-D surface scan in figure 12 (right, green and magenta) for n_{LCFS}=$7 \cdot 10^{18}\mathrm{m}^{-3}$. The increase of impurity radiation by additional seeding results in a strong mitigation of the peak maxima almost in correlation to the power loss fraction of a factor of ≈0.4.

The density dependence of the impurity fluxes achieved by nitrogen and neon puffing is shown in figure 13 (left). The cyan triangles represent the nitrogen flux and the magenta circles correspond to the neon flux. The simultaneous carbon fluxes during nitrogen and neon seeding are given by black triangles and circles, respectively. For comparison the carbon fluxes for scenarios without seeding are shown as grey squares. During seeding with neon or nitrogen the carbon flux drops by ≈11-12%. The resulting total impurity radiation shown in figure 13 (right) consists of the prescribed 1.6MW losses (dashed blue line) by impurity seeding and additional radiative losses from sputtered intrinsic carbon which scales with the limiter recycling fluxes of the considered density scenarios.

The results in figure 13 (left) show unrealistically high seeding rates required for low density plasmas to achieve the 1.6MW radiation losses so that the seeded impurity would dominate over the main hydrogen plasma species (e.g. $I_N \approx 100 \cdot I_C \approx 2.8 \cdot 10^{20}\mathrm{s}^{-1}$ for n_{LCFS}=$1 \cdot 10^{18}\mathrm{m}^{-3}$). Radiative edge cooling with significant power losses appears not to be feasible in the lowest density scenario taken into account here and violates the validity of the trace impurity model applied. With rising n_{LCFS}, the nitrogen fluxes reach the same strength as those from intrinsic carbon. Even lower seeding rates are needed for neon. For example one finds for n_{LCFS}=$1.9 \cdot 10^{19}\mathrm{m}^{-3}$, $I_N \approx I_C \approx 3.2 \cdot 10^{21}\mathrm{s}^{-1}$ and $I_{Ne} \approx 0.3 \cdot I_C \approx 10^{21}\mathrm{s}^{-1}$. This means that in this relevant regime only moderate amounts of nitrogen and neon are needed for achieving significant radiative power losses.

In figure 14 the complete heat flux characteristics are shown for all density scenarios at an input power of 4MW with and without eroded and seeded impurities. The peak heat maxima of the 1-D surface profiles show for left and right peaks a strong drop of 40-50% in case of lower densities once nitrogen or neon are injected (figure 14, left). However, with increasing density the peak heat maxima are less affected by the power dissipation through impurities. The local heat flux decays λ_{sf} shown in figure 14 (right)

are affected even less dramatically by the power dissipation. In spite of the discrete distribution of local gas sources and the helical localization of radiative power losses (figure 10b, c) a homogeneously reduced power load is achieved.

Neon is a more effective radiator compared to nitrogen as it provides more energy levels and achieves the same integrated radiation with less concentration such that $I_{Ne} \approx 0.3 \cdot I_N$. However, it is shown in figure 11d that neon radiation also expands deeper into the confinement region where a change of transport conditions, as demonstrated above for carbon, might also change the SOL radiation fraction $P_{rad,Ne}(r < r_{LCFS})$ significantly. In contrast, nitrogen radiates for the higher densities predominantly in the SOL and the vincinity of the LCFS (figure 11c). Thus, the arguments made for carbon in section 6 regarding the uncertainties in core transport should hold for nitrogen to a large extent. A larger amount of core nitrogen radiation occurs for the lowest density case (figure 11c), but the seeding flux in this case reaches the order of magnitude of the recycling flux of the background hydrogen. As discussed above such scenarios with high impurity content are not desired.

8. Conclusions

A first plasma edge transport study based on 3-D modeling with EMC3-EIRENE and including the effects of impurities is presented for the Wendelstein 7-X limiter startup scenario. It is shown that the limiters cause still a complex, but well defined 3-D magnetic edge topology consisting of helical flux tubes of three different lengths L_C that have a strong impact on the SOL plasma transport.

This topological impact results in a modulation of plasma parameters in correlation with the connection lengths and in the formation of counter streaming flows. This non-uniform edge transport causes unevenly distributed power loads on the limiters, featuring maximum peak loads in the domains where the longest connection length flux tubes connect to the limiter surfaces. The heat load distribution width λ_{sf} on the target surface is defined. It originates from the exponential parallel heat flux decay $\lambda_{q\parallel}$ and modified by the edge magnetic topology and the target geometry function.

A mitigation of peak fluxes and broadening of λ_{sf} can be achieved by increasing the perpendicular to parallel transport ratio. This can be reached in the modeling by either increasing the density n_{LCFS} or, more effectively, by increasing the perpendicular anomalous transport coefficients $D_\perp$, $\chi_{\perp,e,i}$.

Impurity transport was assessed with respect to its feasibility for radiative edge cooling in the 3-D boundary topology. For carbon it is shown that the SOL impurity transport is relatively independent of the transport conditions in the confinement region. However, the total radiative losses can be affected significantly by further ionization in the core region. This implies that for nitrogen and even more for neon, a dedicated choice of core plasma conditions is necessary in order to provide more reliable estimations for the actual amount of radiative losses.

It is shown that intrinsic carbon causes radiative losses of less than 10% of the

input power for the considered density range. Therefore, carbon sputtering alone is not relevant for significant edge cooling and heat load mitigation in the scenarios addressed. Significant radiative losses are instead achieved by seeding nitrogen and neon. Nitrogen and neon fluxes are calculated so that their total radiation is fixed to be 40% of the input power, resulting in a reduction of peak load typically by 40-50%. The volumetric impurity radiation occurs in helical structures due to the local sources, but leads to a quite homogeneous reduction of the power loads on the limiters. This confirms the need for a distribution of gas sources which accounts for the 5/5 symmetric structure of the plasma edge. This is planned for the topologically more complex island divertor operation for which the initial results from the limiter configuration can serve as a guideline.

Acknowledgments: This work was supported in part by the U.S. Department of Energy (DoE) under grant DE-SC0014210 and by start up funds of the Department of Engineering Physics and of the College of Nuclear Engineering at the University of Wisconsin - Madison, USA. The publisher, by accepting the article for publication acknowledges, that the United States Government retains a non-exclusive, paid-up, irrevocable, world-wide license to publish or reproduce the published form of this manuscript, or allow others to do so, for United States Government purposes. This work has been carried out within the framework of the EUROfusion Consortium and has received funding from the Euratom research and training programme 2014-2018 under grant agreement No 633053. The views and opinions expressed herein do not necessarily reflect those of the European Commission. This research was performed using the computer resources and assistance of the UW-Madison Center For High Throughput Computing (CHTC) and the high performance computing system Hydra of the Max-Planck-Society at Rechenzentrum Garching (RZG).

9. References

[1] G. Grieger and I. Milch. Das Fusionsexperiment WENDELSTEIN 7-X. *Physik Journal*, 49(11):1001–1005, 1993.

[2] J. Nührenberg, W. Lotz, P. Merkel, C. Nührenberg, U. Schwenn, E. Strumberger, and T. Hayashi. Overview on Wendelstein 7-X Theory. *Fusion Technology*, 27:71–78, 1995.

[3] T. Sunn Pedersen, T. Andreeva, H.-S. Bosch, S. Bozhenkov, F. Effenberg, M. Endler, Y. Feng, D.A. Gates, J. Geiger, D. Hartmann, H. Hölbe, M. Jakubowski, R. König, H.P. Laqua, S. Lazerson, M. Otte, M. Preynas, O. Schmitz, T. Stange, Y. Turkin, and the W7-X Team. Plans for the first plasma operation of Wendelstein 7-X. *Nuclear Fusion*, 55(12):126001, 2015.

[4] S. Bozhenkov, F. Effenberg, Y. Feng, J. Geiger, D. A. Hartmann, H. Hölbe, T. S. Pedersen, and R. C. Wolf. Limiter for the early operation phase of W7-X. In S. Ratynskaia, P. Mantica, A. Benuzzi-Mounaix, G. Dilecce, R. Bingham, M. Hirsch, B. Kemnitz, and T. Klinger, editors, *41st EPS Conference on Plasma Physics*, volume 38F of *Europhysics Conference Abstracts (ECA)*, Berlin, 2014.

[5] C. D. Beidler, E. Harmeyer, J. Kisslinger, F. Rau, H. Renner, and H. Wobig. Island Divertor Concept for the Stellarator Wendelstein 7-X. In J. A. C. Cabral, M. E. Manso, and F. M. Serra, editors, *ECA*, volume 17C, Part 2, pages 787–790, Lisbon, 1993. European Physical Society.

[6] D. Sharma, Y. Feng, and F. Sardei. A 3D Monte-Carlo study of the W7-X island divertor transport for different magnetic configurations. *Nuclear Fusion*, 46:S127–S138, 2006.

[7] Y. Feng, J. Kisslinger, F. Sardei, and D. Reiter. EMC3/EIRENE Transport Modelling of the Island Divertor in W7-X. In P. Lalousis and S. Moustaizis, editors, *35th European Physical Society Conference on Plasma Physics and 10th International Workshop on Fast Ignition of Fusion Targets. Contributed Papers*, volume 32D of *ECA*, Hersonissos, Crete, 2008. European Physical Society.

[8] F. Nguyen, P. Chendrih, and A. Grosman. Interaction of stochastic boundary layer with plasma facing components. *Nuclear Fusion*, 37(6):743, 1997.

[9] Ph. Ghendrih, M. Becoulet, L. Colas, A. Grosman, R. Guirlet, J. Gunn, T. Loarer, A. Azéroual, V. Basiuk, B. Beaumont, A. Bécoulet, P. Beyer, S. Brémond, J. Bucalossi, H. Capes, Y. Corre, L. Costanzo, C. De Michelis, P. Devynck, S. Féron, C. Friant, X. Garbet, R. Giannella, C. Grisolia, W. Hess, J. Hogan, L. Ladurelle, F. Laugier, G. Martin, M. Mattioli, B. Meslin, P. Monier-Garbet, D. Moulin, F. Nguyen, J.-Y. Pascal, A.-L. Pecquet, B. Pégourié, R. Reichle,

F. Saint-Laurent, J.-C. Vallet, M. Zabiégo, and Tore Supra Teams. Progress in ergodic divertor operation on Tore Supra. *Nuclear Fusion*, 42(10):1221, 2002.

[10] O. Schmitz, M.W. Jakubowski, H. Frerichs, D. Harting, M. Lehnen, B. Unterberg, S.S. Abduallaev, S. Brezinsek, I. Classen, T. Evans, Y. Feng, K.H. Finken, M. Kantor, D. Reiter, U. Samm, B. Schweer, G. Sergienko, G.W. Spakman, M. Tokar, E. Uzgel, R.C. Wolf, and the TEXTOR Team. Identification and analysis of transport domains in the stochastic boundary of TEXTOR-DED for different mode spectra. *Nuclear Fusion*, 48(2):024009, 2008.

[11] T. Eich, D. Reiser, and K.H. Finken. Two dimensional modelling approach to transport properties of the TEXTOR-DED laminar zone. *Nuclear Fusion*, 40(10):1757, 2000.

[12] M. W. Jakubowski, O. Schmitz, S. S. Abdullaev, S. Brezinsek, K. H. Finken, A. Krämer-Flecken, M. Lehnen, U. Samm, K. H. Spatschek, B. Unterberg, and R. C. Wolf. Change of the Magnetic-Field Topology by an Ergodic Divertor and the Effect on the Plasma Structure and Transport. *Phys. Rev. Lett.*, 96:035004, Jan 2006.

[13] T. Morisaki, S. Masuzaki, M. Kobayashi, M. Shoji, J. Miyazawa, R. Sakamoto, G. Motojima, M. Goto, H. Funaba, H. Tanaka, K. Tanaka, I. Yamada, S. Ohdachi, H. Yamada, A. Komori, and the LHD Experiment Group. Initial experiments towards edge plasma control with a closed helical divertor in LHD. *Nuclear Fusion*, 53(6):063014, 2013.

[14] M. Kobayashi, Y. Xu, K. Ida, Y. Corre, Y. Feng, O. Schmitz, H. Frerichs, F.L. Tabares, T.E. Evans, J.W. Coenen, Y. Liang, A. Bader, K. Itoh, H. Yamada, Ph. Ghendrih, G. Ciraolo, D. Tafalla, A. Lopez-Fraguas, H.Y. Guo, Z.Y. Cui, D. Reiter, N. Asakura, U. Wenzel, S. Morita, N. Ohno, B.J. Peterson, and S. Masuzaki. 3D effects of edge magnetic field configuration on divertor/scrape-off layer transport and optimization possibilities for a future reactor. *Nuclear Fusion*, 55(10):104021, 2015.

[15] A. Bader, D. T. Anderson, C. C. Hegna, Y. Feng, J. D. Lore, and J. N. Talmadge. Simulations of edge configurations in quasi-helically symmetric geometry using EMC3-EIRENE. *Nuclear Fusion*, 53, 2013.

[16] A. R. Akerson, A. Bader, C. C. Hegna, O. Schmitz, L. A. Stephey, D. T. Anderson, F. S. B. Anderson, and K. M. Likin. Three-dimensional scrape off layer transport in the helically symmetric experiment HSX. *Plasma Physics and Controlled Fusion*, 58(8):084002, 2016.

[17] J. Geiger, R. C. Wolf, C. Beidler, A. Cardella, E. Chlechowitz, V. Erckmann, G. Gantenbein, D. Hathiramani, M. Hirsch, W. Kasparek, J. Kilinger, R. Knig, P. Kornejew, H. P. Laqua, C. Lechte, J. Lore, A. Lumsdaine, H. Maaberg, N. B. Marushchenko, G. Michel, M. Otte, A. Peacock, T. Sunn Pedersen, M. Thumm, Y. Turkin, A. Werner, D. Zhang, and the W7-X Team. Aspects of steady-state operation of the Wendelstein 7-X stellarator. *Plasma Physics and Controlled Fusion*, 55(1):014006, 2013.

[18] Y. Feng. Up-scaling the island divertor along the W7-stellarator line. *Journal of Nuclear Materials*, 438, Supplement:S497–S500, 2013. Proceedings of the 20th International Conference on Plasma-Surface Interactions in Controlled Fusion Devices.

[19] H. Hölbe, T. Sunn Pedersen, J. Geiger, S. Bozhenkov, R. König, Y. Feng, J. Lore, A. Lumsdaine, and the Wendelstein 7-X Team. Access to edge scenarios for testing a scraper element in early operation phases of Wendelstein 7-X. *Nuclear Fusion*, 56(2):026015, 2016.

[20] U. Samm, G. Bertschinger, P. Bogen, J. D. Hey, E. Hintz, L. Konen, Y. T. Lie, A. Pospieszczyk, D. Rusbuldt, R. P. Schorn, B. Schweer, M. Tokar, and B. Unterberg. Radiative edges under control by impurity fluxes. *Plasma Physics and Controlled Fusion*, 35(SB):B167, 1993.

[21] J. Rapp, P. Monier-Garbet, G.F. Matthews, R. Sartori, P. Andrew, P. Dumortier, T. Eich, W. Fundamenski, M. von Hellermann, J. Hogan, L.C. Ingesson, S. Jachmich, H.R. Koslowski, A. Loarte, G. Maddison, D.C. McDonald, A. Messiaen, J. Ongena, V. Parail, V. Philipps, G. Saibene, B. Unterberg, and JET EFDA Contributors. Reduction of divertor heat load in JET ELMy H-modes using impurity seeding techniques. *Nuclear Fusion*, 44(2):312, 2004.

[22] T.W. Petrie, G.D. Porter, N.H. Brooks, M.E. Fenstermacher, J.R. Ferron, M. Groth, A.W. Hyatt, R.J. La Haye, C.J. Lasnier, A.W. Leonard, T.C. Luce, P.A. Politzer, M.E. Rensink, M.J.

Schaffer, M.R. Wade, J.G. Watkins, and W.P. West. Impurity behaviour under puff-and-pump radiating divertor conditions. *Nuclear Fusion*, 49(6):065013, 2009.

[23] A. Kallenbach, M. Balden, R. Dux, T. Eich, C. Giroud, A. Huber, G.P. Maddison, M. Mayer, K. McCormick, R. Neu, T.W. Petrie, T. Ptterich, J. Rapp, M.L. Reinke, K. Schmid, J. Schweinzer, and S. Wolfe. Plasma surface interactions in impurity seeded plasmas. *Journal of Nuclear Materials*, 415(1, Supplement):S19 – S26, 2011. Proceedings of the 19th International Conference on Plasma-Surface Interactions in Controlled Fusion.

[24] M.L. Reinke, J.W. Hughes, A. Loarte, D. Brunner, I.H. Hutchinson, B. LaBombard, J. Payne, and J.L. Terry. Effect of N2, Ne and Ar seeding on Alcator C-Mod H-mode confinement. *Journal of Nuclear Materials*, 415(1, Supplement):S340 – S344, 2011. Proceedings of the 19th International Conference on Plasma-Surface Interactions in Controlled Fusion.

[25] G.P. Maddison, C. Giroud, G.K. McCormick, J.A. Alonso, B. Alper, G. Arnoux, P.C. da Silva Aresta Belo, M.N.A. Beurskens, A. Boboc, S. Brezinsek, I. Coffey, S. Devaux, T. Eich, W. Fundamenski, D. Harting, A. Huber, S. Jachmich, I. Jenkins, E. Joffrin, M.A.H. Kempenaars, M. Lehnen, T. Loarer, P.J. Lomas, A.G. Meigs, P.D. Morgan, V. Riccardo, F.G. Rimini, M.F. Stamp, G. Telesca, H. Thomsen, and JET EFDA contributors. Moderation of divertor heat loads by fuelling and impurity seeding in well-confined ELMy H-mode plasmas on JET. *Nuclear Fusion*, 51(4):042001, 2011.

[26] J. D. Lore, M. L. Reinke, D. Brunner, B. LaBombard, B. Lipschultz, J. Terry, R. A. Pitts, and Y. Feng. Three-dimensional simulation of H-mode plasmas with localized divertor impurity injection on Alcator C-Mod using the edge transport code EMC3-EIRENE. *Physics of Plasmas*, 22(5), 2015.

[27] T. Morisaki, K. Oyama, N. Tamura, S. Masuzaki, T. Akiyama, G. Motojima, J. Miyazawa, B.J. Peterson, N. Ohno, and H. Yamada. Radiated power distributions in impurity-seeded plasmas in LHD. *Journal of Nuclear Materials*, 463:640 – 643, 2015. 21Proceedings of the 21st International Conference on Plasma-Surface Interactions in Controlled Fusion Devices Kanazawa, Japan May 26-30, 2014.

[28] T.E. Evans, M. Goniche, A. Grosman, D. Guilhem, W. Hess, and J.-C. Vallet. Plasma-Surface Interactions in Controlled Fusion Devices Magnetic perturbation effects on boundary plasmas during high power lower hybrid current drive in Tore Supra. *Journal of Nuclear Materials*, 196:421 – 425, 1992.

[29] Y. Feng, F. Sardei, J. Kisslinger, P. Grigull, K. McCormick, D. Reiter, L. Giannone, R. König, N. Ramasubramanian, H. Thomsen, and U. Wenzel. Physics of the geometry-related detachment stability in W7-AS. *Nuclear Fusion*, 45(2):89, 2005.

[30] P. Grigull, K. McCormick, Y. Feng, A. Werner, R. Brakel, H. Ehmler, F. Gadelmeier, D. Hartmann, D. Hildebrandt, R. Jaenicke, J. Kisslinger, T. Klinger, R. König, D. Naujoks, H. Niedermeyer, N. Ramasubramanian, F. Sardei, F. Wagner, and U. Wenzel. Influence of magnetic field configurations on divertor plasma parameters in the W7-AS stellarator. *Journal of Nuclear Materials*, 313316:1287 – 1291, 2003. Plasma-Surface Interactions in Controlled Fusion Devices 15.

[31] M. Kobayashi, S. Masuzaki, I. Yamada, Y. Narushima, C. Suzuki, N. Tamura, B.J. Peterson, S. Morita, C.F. Dong, N. Ohno, S. Yoshimura, Y. Feng, M. Goto, K. Sato, T. Akiyama, K. Tanaka, and the LHD experiment group. Control of 3D edge radiation structure with resonant magnetic perturbation fields applied to the stochastic layer and stabilization of radiative divertor plasma in LHD. *Nuclear Fusion*, 53(9):093032, 2013.

[32] R. König, J. Baldzuhn, W. Biel, C. Biedermann, H.S. Bosch, S. Bozhenkov, T. Bruer, B. Brotas de Carvalho, R. Burhenn, B. Buttenschön, G. Cseh, A. Czarnecka, M. Endler, V. Erckmann, T. Estrada, J. Geiger, O. Grulke, D. Hartmann, D. Hathiramani, M. Hirsch, S. Jabonski, M. Jakubowski, J. Kaczmarczyk, T. Klinger, S. Klose, G. Kocsis, P. Kornejew, A. Krmer-Flecken, T. Kremeyer, M. Krychowiak, M. Kubkowska, A. Langenberg, H. P. Laqua, M. Laux, Y. Liang, A. Lorenz, A.O. Marchuk, V. Moncada, O. Neubauer, U. Neuner, J.W. Oosterbeek,

M. Otte, N. Pablant, E. Pasch, T.S. Pedersen, K. Rahbarnia, L. Ryc, O. Schmitz, W. Schneider, H. Schuhmacher, B. Schweer, T. Stange, H. Thomsen, J.-M. Travere, T. Szepesi, U. Wenzel, A. Werner, B. Wiegel, T. Windisch, R. Wolf, G.A. Wurden, D. Zhang, A. Zimbal, S. Zoletnik, and the W7-X Team. The Set of Diagnostics for the First Operation Campaign of the Wendelstein 7-X Stellarator. *Journal of Instrumentation*, 10(10):P10002, 2015.

[33] H. Frerichs, F. Effenberg, O. Schmitz, C. Biedermann, Y. Feng, M. Jakubowski, R. König, M. Krychowiak, J. Lore, H. Niemann, T. S. Pedersen, L. Stephey, G. A. Wurden, and W7-X Team. Synthetic plasma edge diagnostics in EMC3-EIRENE, highlighted for Wendelstein 7-X, 2016.

[34] Feng Y. et al. 3D Edge Modeling and Island Divertor Physics. *Contributions to Plasma Physics, vol. 44, issue 13, pp. 57-69*, 44:57–69, apr 2004.

[35] Y. Feng, H. Frerichs, M. Kobayashi, A. Bader, F. Effenberg, D. Harting, H. Hoelbe, J. Huang, G. Kawamura, J. D. Lore, T. Lunt, D. Reiter, O. Schmitz, and D. Sharma. Recent Improvements in the EMC3-EIRENE Code. volume 54, pages 426–431, Cracow, 2014. Akademie-Verlag.

[36] Y. Feng, F. Sardei, and J. Kisslinger. 3D Fluid Modelling of the Edge Plasma by Means of a Monte Carlo Technique. *Journal of Nuclear Materials*, 266-269:812–818, 1999.

[37] D. Reiter. Randschicht-Konfiguration von Tokamaks: Entwicklung und Anwendung stochastischer Modelle zur Beschreibung des Neutralgastransports. *Technical Report Jül-1947*, 1984.

[38] D. Reiter, M. Baelmans, and P. Börner. The EIRENE and B2-EIRENE codes. *Fusion Science and Technology*, 47:172 – 186, 2005. Record converted from VDB: 12.11.2012.

[39] Y. Feng, F. Sardei, J. Kisslinger, D. Reiter, and Yu. L. Igitkhanov. Numerical Studies on Impurity Transport in the W7-AS Island Divertor. In C. Silva, C. Varandas, and D. Campbell, editors, *28th EPS Conference on Controlled Fusion and Plasma Physics. Contributed Paper*, volume 25A of *ECA*, pages 1949–1952, Funchal, 2001. European Physical Society.

[40] G. Grieger, C. Beidler, E. Harmeyer, W. Lotz, J. Kisslinger, P. Merkel, J. Nührenberg, F. Rau, E. Strumberger, and H. Wobig. Modular Stellarator Reactors and Plans for Wendelstein 7-X. *Fusion Technology*, 21(3):1767–1778, 1992.

[41] P. C. Stangeby, J. A. Tagle, S. K. Erents, and C. Lowry. Measurements of the cross-field diffusion coefficient D in the edge plasma of JET. *Plasma Physics and Controlled Fusion*, 30(12):1787, 1988.

[42] Y. Feng, T. Lunt, F. Sardei, and X. Zha. Implicit coupling of impurity transport at the SOL-core interface. *Computer Physics Communications*, 184(6):1555 – 1561, 2013.

[43] M. Kobayashi, Y. Feng, A. Loarte, G. Federici, G. Strohmayer, M. Shimada, F. Sardei, D. Reiter, and M. Sugihara. 3D edge transport analysis of ITER start-up configuration for limiter power load assessment. *Nuclear Fusion*, 47(2):61, 2007.

[44] P.C. Stangeby. A three-dimensional analytic model for discrete limiters in ITER. *Nuclear Fusion*, 50(3):035013, 2010.

[45] P. C. Stangeby. *The Plasma Boundary of Magnetic Fusion Devices*. Plasma Physics Series. Nicki Dennis, 2000.

[46] T. Eich, B. Sieglin, A. Scarabosio, W. Fundamenski, R. J. Goldston, and A. Herrmann. Inter-ELM Power Decay Length for JET and ASDEX Upgrade: Measurement and Comparison with Heuristic Drift-Based Model. *Phys. Rev. Lett.*, 107:215001, Nov 2011.

[47] R.J. Goldston. Heuristic drift-based model of the power scrape-off width in low-gas-puff H-mode tokamaks. *Nuclear Fusion*, 52(1):013009, 2012.

[48] P.C. Stangeby, C.S. Pitcher, and J.D. Elder. The nature of plasma fluxes to surfaces nearly tangential to the magnetic field. *Nuclear Fusion*, 32(12):2079, 1992.

[49] Y. Feng, S. Bozhenkov, F. Effenberg, H. Hölbe, D. Reiter, and Y. Turkin. Neutral transport behavior expected for the first limiter plasmas in W7-X. In S. Ratynskaia, P. Mantica, A. Benuzzi-Mounaix, G. Dilecce, R. Bingham, M. Hirsch, B. Kemnitz, and T. Klinger, editors, *41st EPS Conference on Plasma Physics*, volume 38F of *Europhysics Conference Abstracts (ECA)*, Berlin, 2014.

[50] H. P. Summers. *Atomic data and analysis structure: user manual.* Joint European Torus, Abingdon, 1994.

Figures

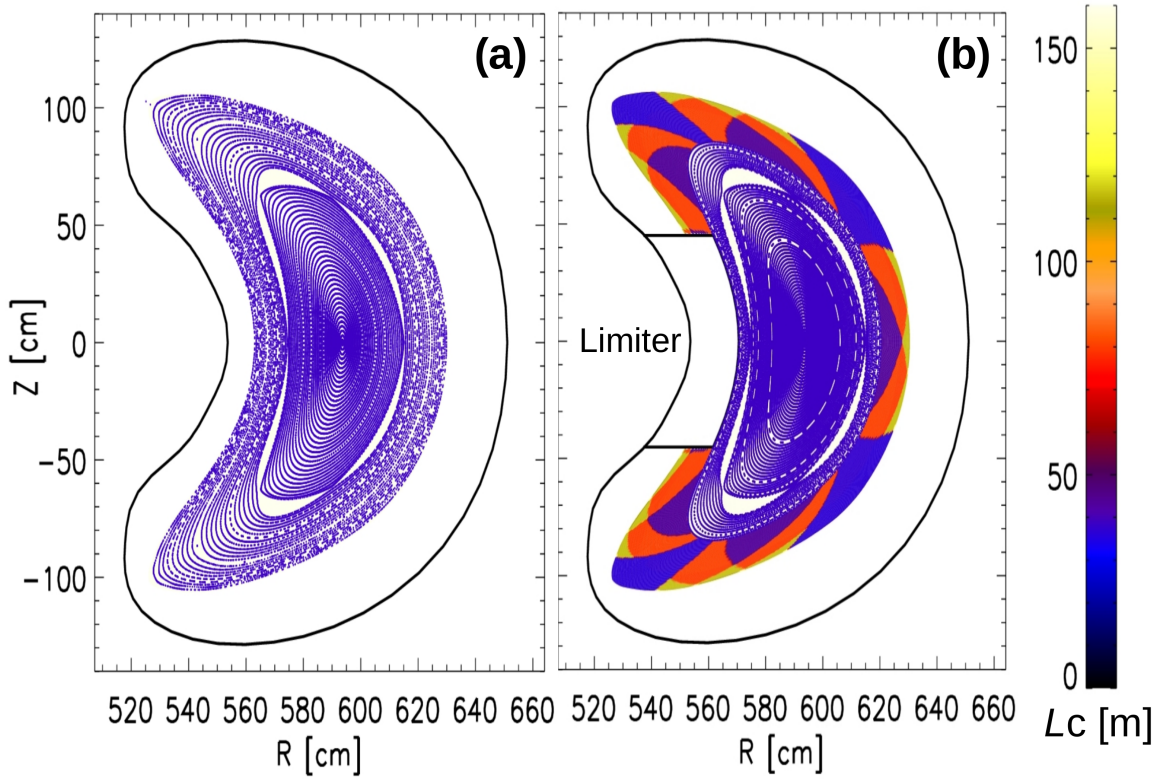

Figure 1: (a) Poincare plot of the vacuum magnetic field at the bean shaped symmetry plane ($\phi_{tor} = 0°$) within the vessel (black solid line). (b) Target-to-target connection lengths (L_C) topology arising once the five graphite inboard limiters inserted open the field lines of the boundary magnetic field. The SOL domain relevant for plasma transport consists of three L_C: 36m (blue), 43m (purple) and 79m (orange).

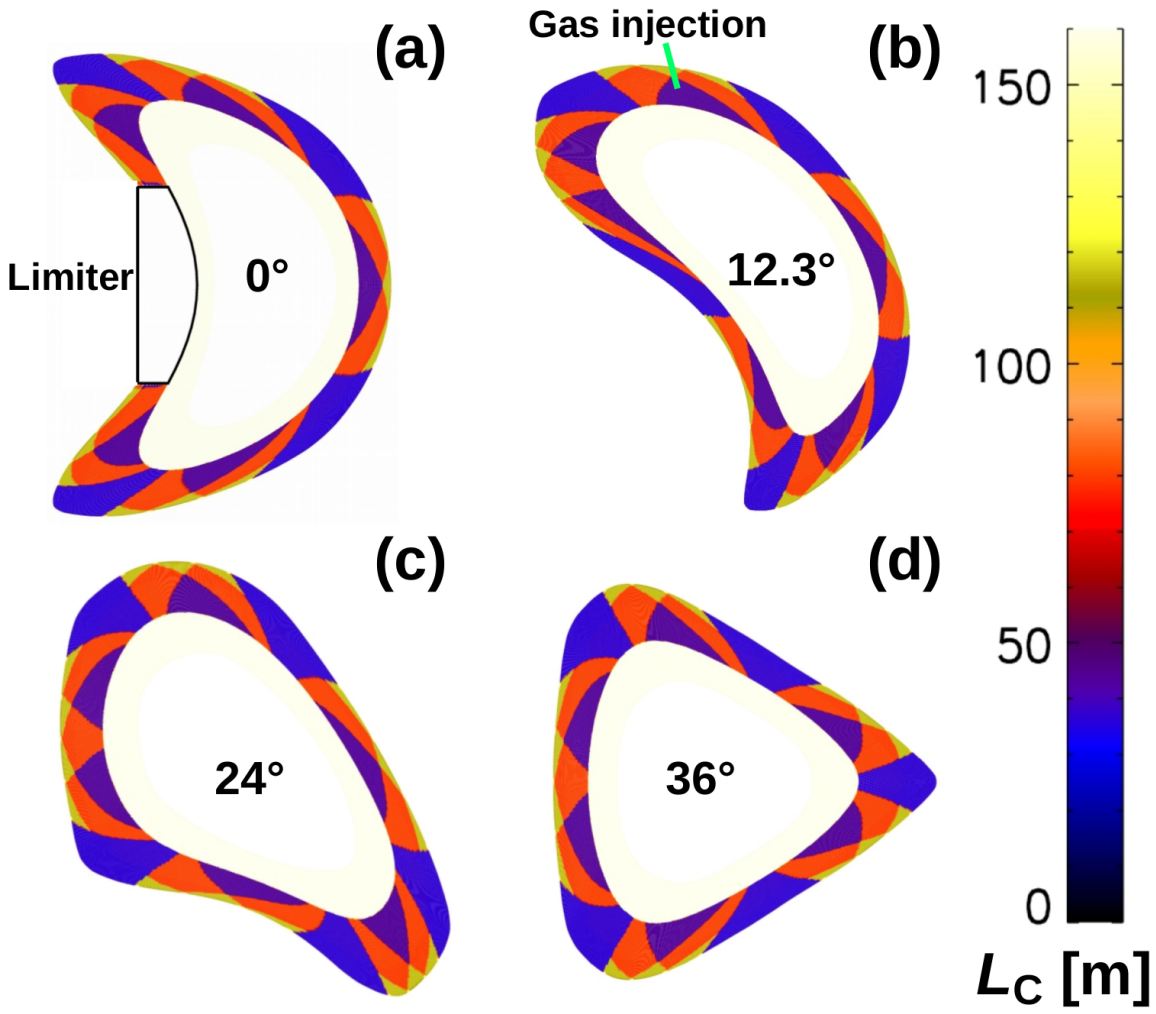

Figure 2: Target-to-target connection lengths (L_C) profiles covering a half field period ($\Delta\phi_{tor} = \frac{1}{2} \cdot \frac{360°}{5} = 36°$) (a) at the bean shaped symmetry plane ($\phi_{tor} = 0°$, including the limiter), (b) the cross section of the impurity seeding source ($\phi_{tor} = 12.3°$, green mark: poloidal seeding position), (c) a cross section at $\phi_{tor} = 24°$, (d) the triangular symmetry plane at $\phi_{tor} = 36°$.

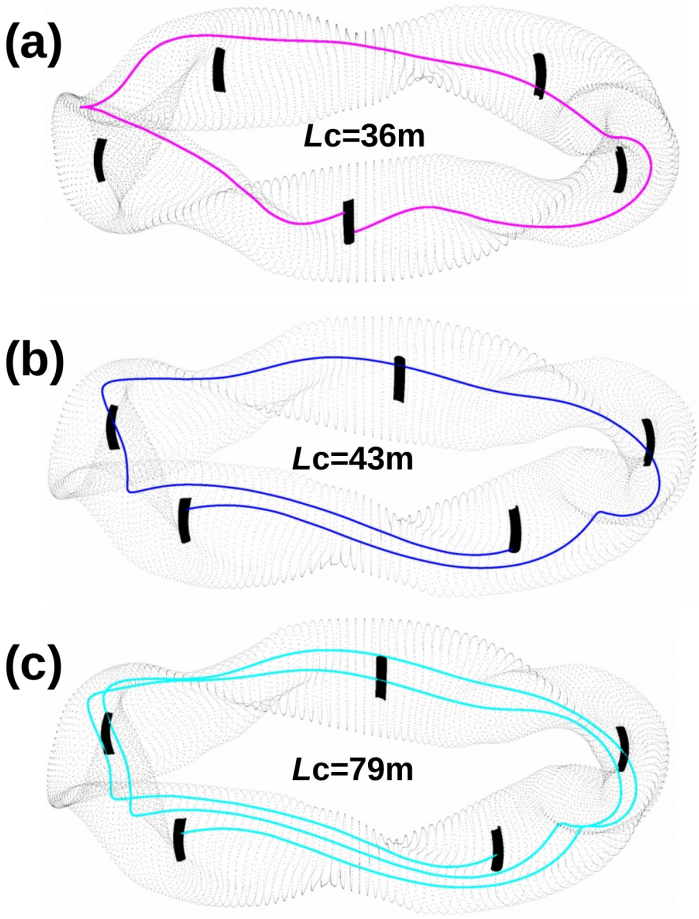

Figure 3: Magnetic field lines representing the three different types of magnetic flux bundles in the SOL. (a) A field line starts on a limiter and hits the same limiter after one toroidal turn (1 turn, $L_C \approx 36$m). (b) A field line starts on a limiter and hits after one toroidal turn the next neighbouring limiter (1.2 turns, $L_C \approx 43$m). (c) A field line starting on one limiter performs two toroidal turns until hitting the next neighbouring limiter (2.2 turns, $L_C \approx 79$m).

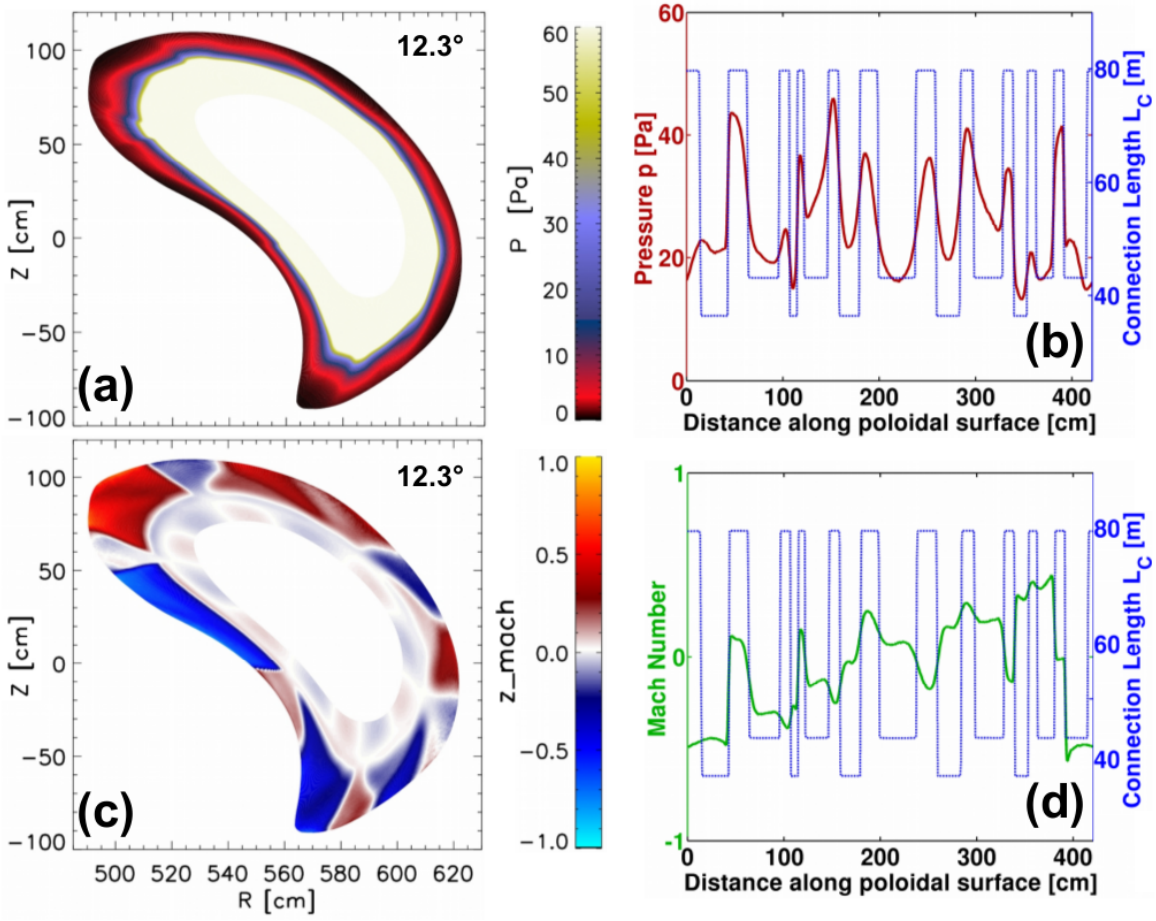

Figure 4: Plasma profiles for $n_{LCFS} = 7{\cdot}10^{18}\mathrm{m}^{-3}$, $P_{in} = 4MW$ at ϕ_{tor} =12.3°: (a) 2-D Pressure profile. (b) 1-D poloidal pressure and connection lengths profile. (c) 2-D Mach number profile. (d) 1-D poloidal Mach number and connection lengths profile.

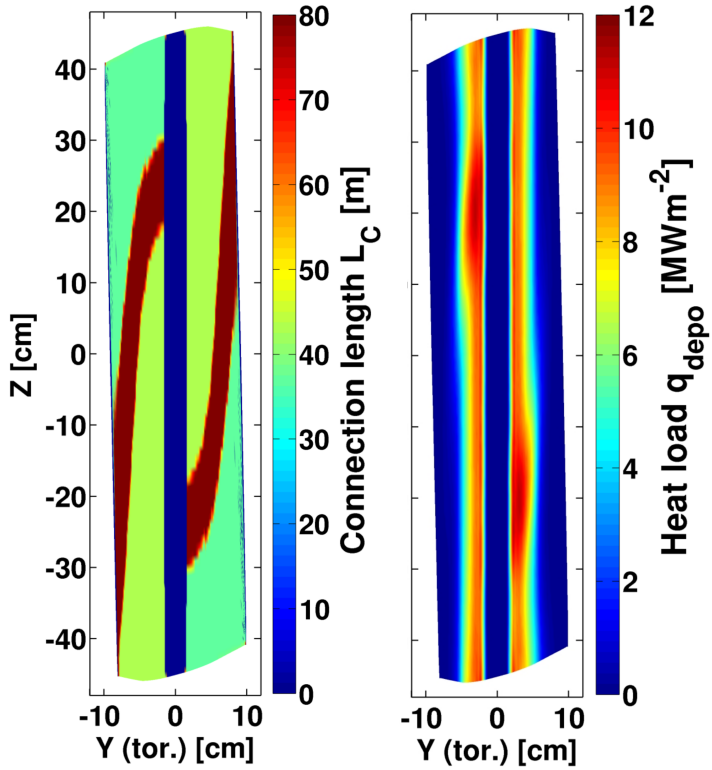

Figure 5: Left: Target-to-target connection length L_C mapped on the limiter. Right: 2-D limiter heat flux deposition for a hydrogen plasma at P_{in} =4MW and $n_{LCFS} = 1 \cdot 10^{18}\mathrm{m}^{-3}$.

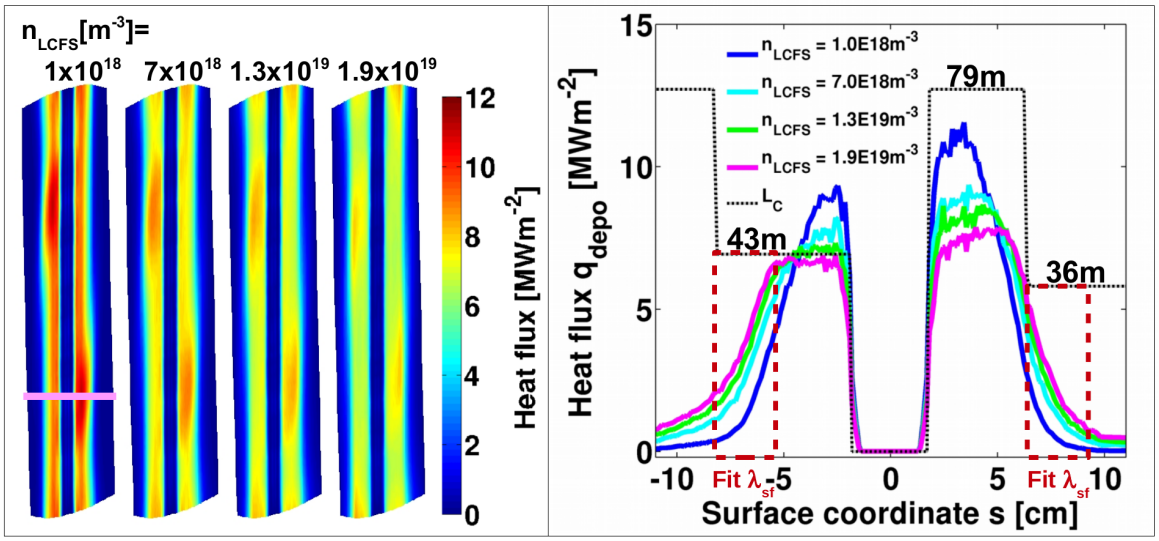

Figure 6: Left: 2-D limiter heat flux deposition for a density scan with pure hydrogen for a density range $n_{LCFS} = 1 \cdot 10^{18}\mathrm{m}^{-3}$ to $1.9{\cdot}10^{19}\mathrm{m}^{-3}$ at P_{in} =4MW. Right: 1-D surface profile of the deposited heat loads extracted at $Z = -0.2$m, magenta mark, left. The overlaid black dotted line corresponds to the according local L_C. The red dotted box indicates the fit domain for λ_{sf}.

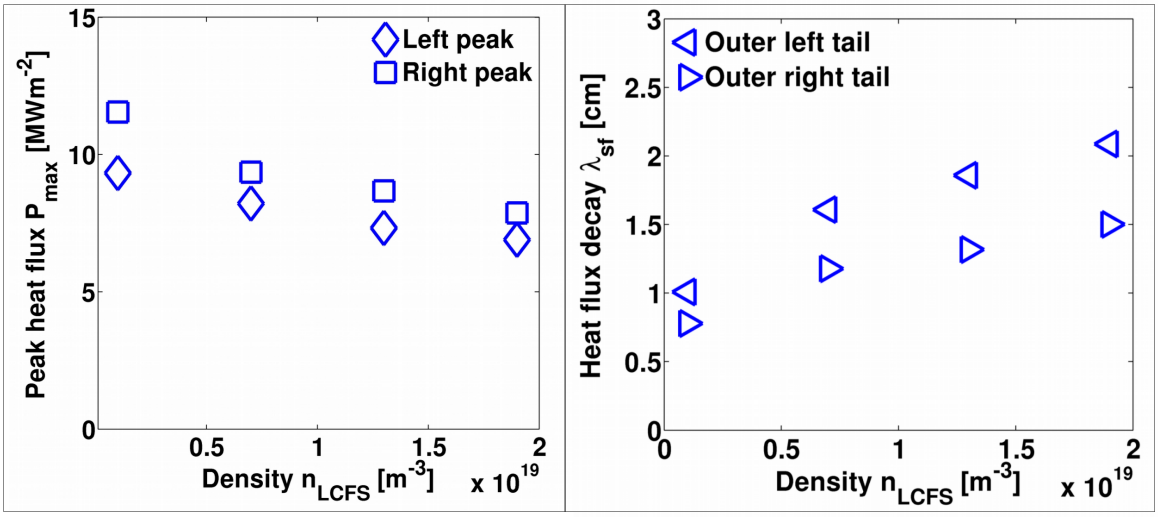

Figure 7: Left: Maximum deposited peak heat fluxes P_{peak} and right: limiter surface deposition decay lengths λ_{sf} for four different density cases $n_{LCFS} = 1 \cdot 10^{18}$, $7 \cdot 10^{18}$, $1.3 \cdot 10^{19}$ and $1.9 \cdot 10^{19}\mathrm{m}^{-3}$ at $P_{in} = 4MW$ inferred from the 1-D profiles in figure 6.

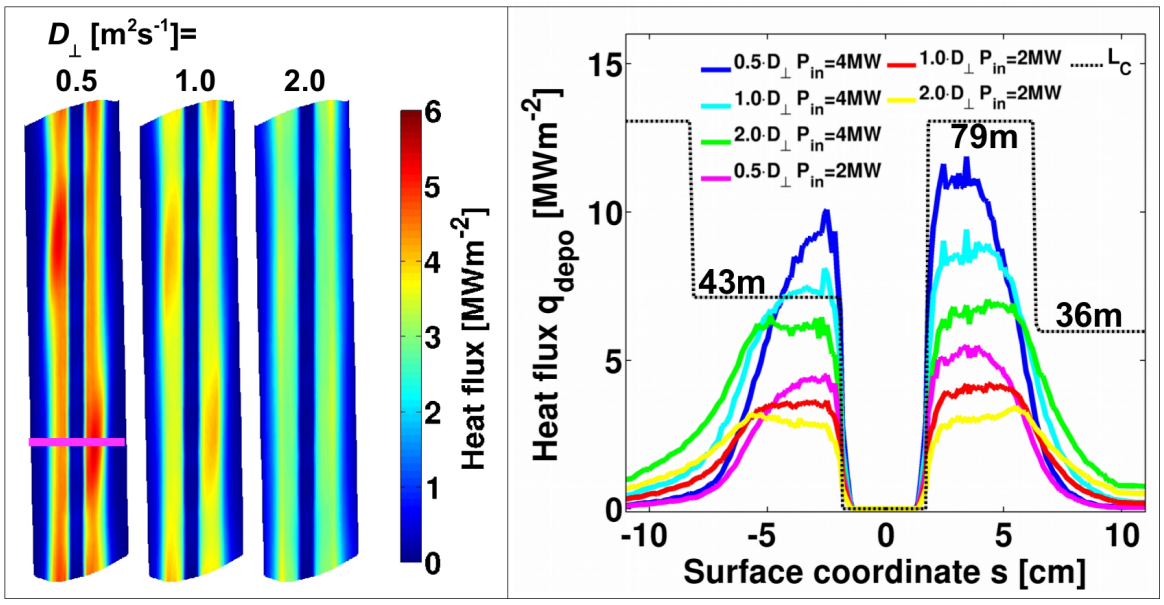

Figure 8: Left: 2-D limiter heat flux deposition for a transport parameter scan for a pure hydrogen plasma at $n_{LCFS} = 9 \cdot 10^{18}\mathrm{m}^{-3}$, $P_{in} = 2MW$, $D_\perp = 0.5$, 1.0, $2.0\mathrm{m}^2\mathrm{s}^{-1}$, $\chi_{\perp,e,i} = 3D_\perp$. Right: 1-D surface scan of the deposited heat flux at $Z = -0.2$m for a transport and power parameter scan at $n_{LCFS} = 9 \cdot 10^{18}\mathrm{m}^{-3}$, P_{in} =2MW, 4MW, $D_\perp$ =0.5, 1.0, $2.0\mathrm{m}^2\mathrm{s}^{-1}$, $\chi_{\perp,e,i} = 3D_\perp$ extracted at $Z = -0.2$m, magenta mark, left.

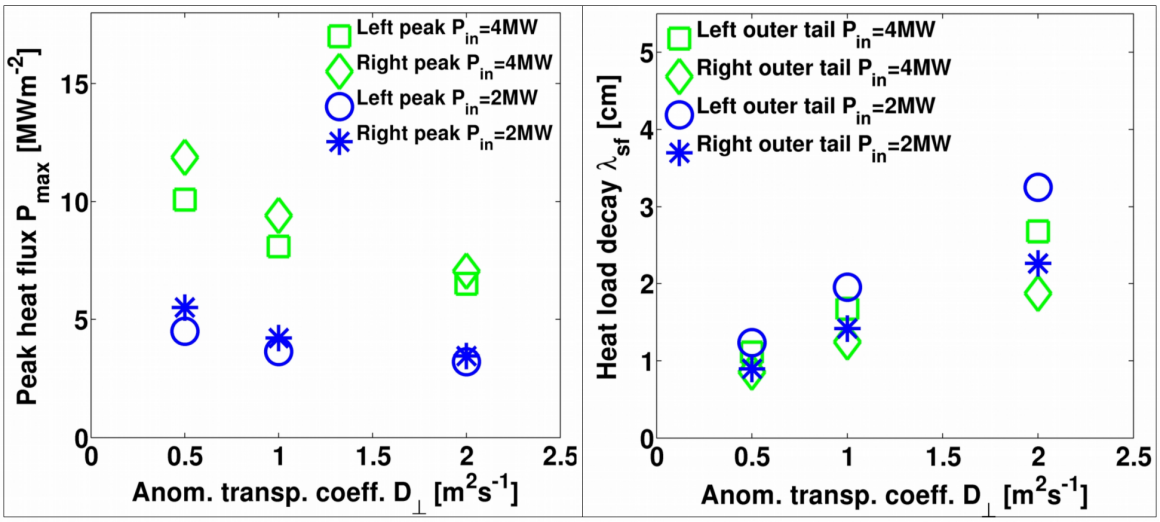

Figure 9: Left: Maximum deposited peak heat fluxes P_{peak} and right: limiter surface deposition decay lengths λ_{sf} for three different spatially fixed anomalous transport coefficients $D_\perp$ ($\chi_{perp,e,i} = 3D_\perp$) for $n_{LCFS} = 9 \cdot 10^{18}\mathrm{m}^{-3}$ at P_{in} = 2MW, 4MW respectively, inferred from the 1-D profiles in figure 8.

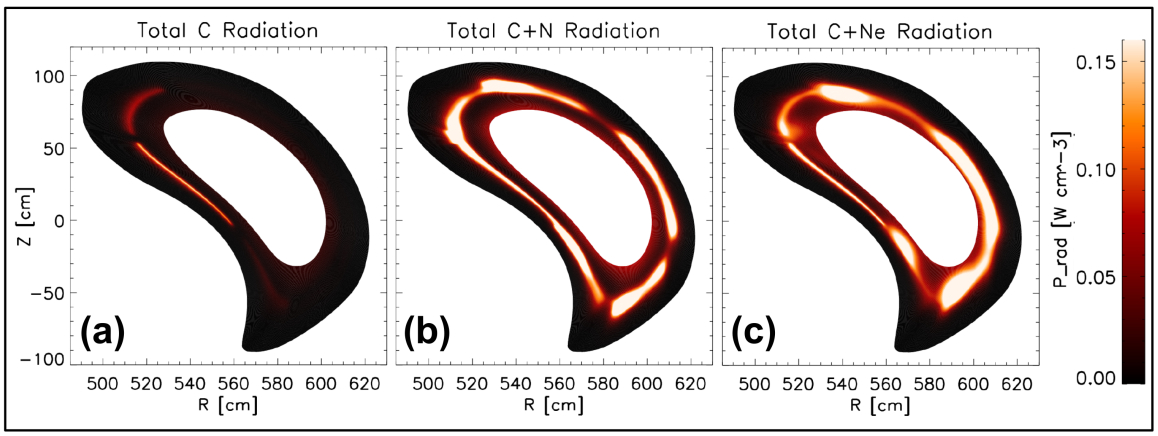

Figure 10: 2-D total impurity radiation profiles at $\phi_{tor} = 12.3°$ for (a) intrinsic carbon eroded from the limiter, (b) seeded nitrogen (including intrinsic carbon), (c) seeded neon (including intrinsic carbon) at $n_{LCFS} = 7{\cdot}10^{19}\mathrm{m}^{-3}$ at P_{in} =4MW. Nitrogen and neon are injected at the top (compare with figure 2b).

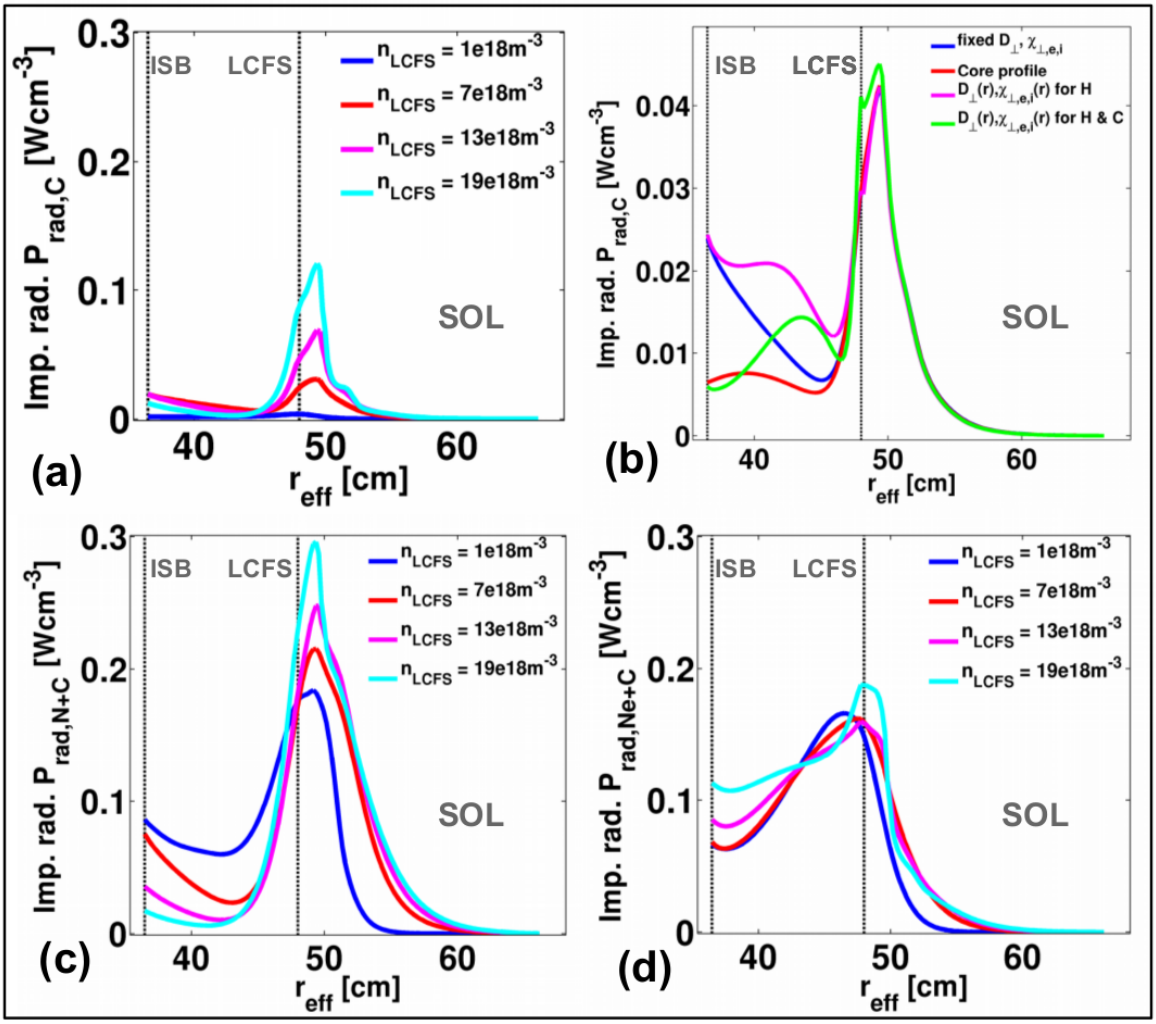

Figure 11: Radial distribution of total impurity radiation for the density scan at P_{in} =4MW. (a) Intrinsic carbon eroded from the limiter, (b) intrinsic carbon for different transport conditions at fixed $n_{LCFS} = 9{\cdot}10^{19}\mathrm{m}^{-3}$, (c) seeded nitrogen (including intrinsic carbon), (d) seeded neon (including intrinsic carbon). The black dotted lines indicate ISB and LCFS (relevant for the boundary conditions).

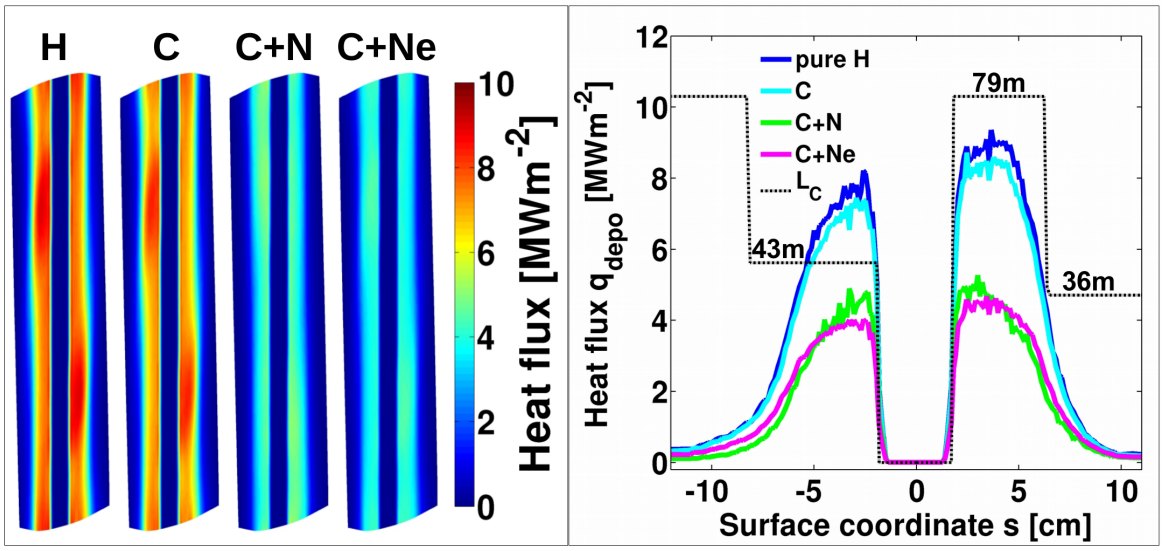

Figure 12: Left: 2-D limiter heat loads for $n_{LCFS} = 7 \cdot 10^{19}\mathrm{m}^{-3}$, P_{in} =4MW for pure hydrogen (H), including power losses due to sputtered carbon (C), additional nitrogen seeding (C+N) and additional neon seeding (C+Ne). Right: the resulting 1-D surface profiles for pure hydrogen and diluted plasmas at $Z = -0.2m$ (compare mark in figure 6).

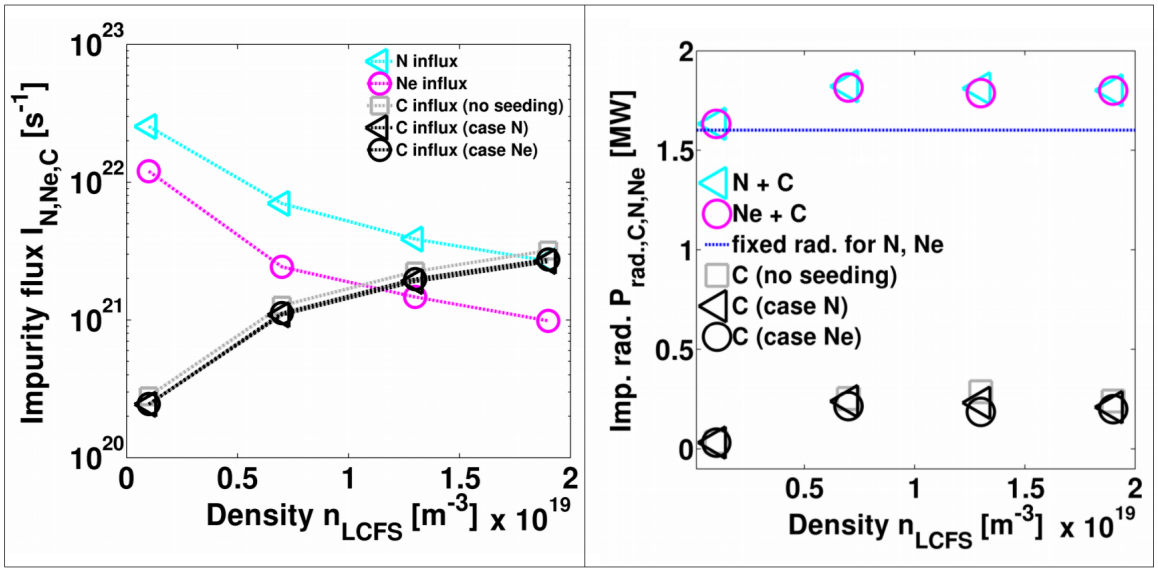

Figure 13: Left: impurity influxes for nitrogen (cyan triangles) and simultaneously eroded carbon (black triangles), neon (magenta circles) and simultaneously eroded carbon (black circles) and eroded carbon without seeding (grey squares) for different n_{LCFS}. Right: total impurity radiation caused by the fluxes shown on the left for seeded nitrogen and eroded carbon (cyan triangles), neon and eroded carbon (magenta circles) and impurity losses in case of eroded carbon without seeding (grey squares) and the respective radiation fractions due to carbon erosion only in case of seeded nitrogen (black triangles) and neon (black circles). The blue dotted line marks the fixed radiation fraction of the seeded species.

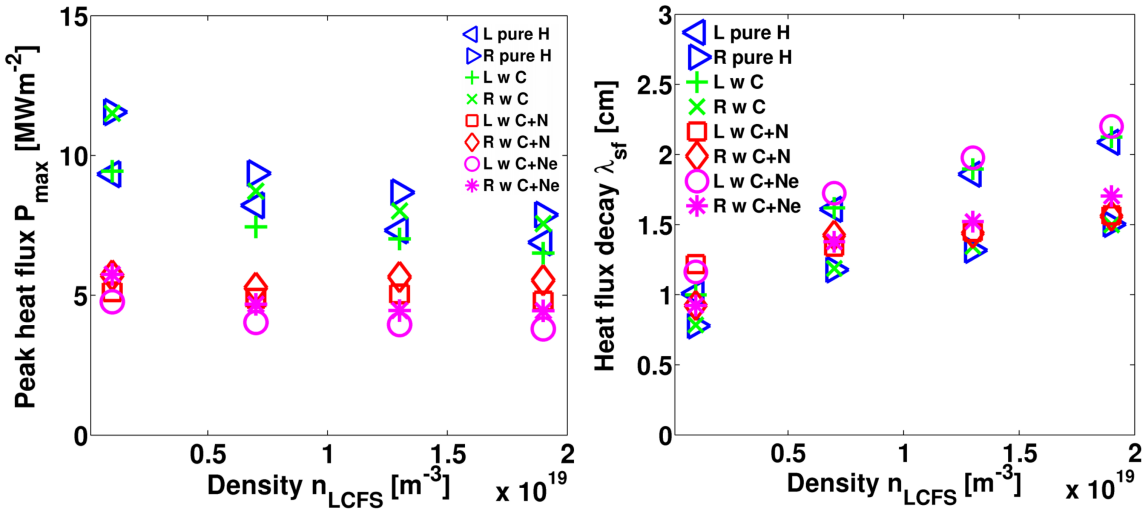

Figure 14: Left: Peak heat fluxes P_{peak} and right: limiter surface deposition decay lengths λ_{sf} for different n_{LCFS} for hydrogen plasmas (blue triangles), including intrinsic sputtered carbon impurities (green +- and x-symbols), additional seeding of nitrogen (red diamonds and squares) and neon (magenta circles and stars).